FeIII-substituted brucite: Hydrothermal synthesis from (Mg0.8FeII0.2)-brucite, crystal chemistry and relevance to the alteration of ultramafic rocks

William Carlin, Benjamin Malvoisin, Bruno Lanson, Fabrice Brunet, Nathaniel Findling, Martine Lanson, Valérie Magnin, Tiphaine Fargetton, Laurent Jeannin, Olivier Lhote

Fe^{III}-substituted brucite: hydrothermal synthesis from $(Mg_{0.8},Fe^{II}_{0.2})$-brucite, crystal chemistry and relevance to the alteration of ultramafic rocks

William Carlin[1,2], Benjamin Malvoisin[1], Bruno Lanson[1], Fabrice Brunet[1], Nathaniel Findling[1], Martine Lanson[1], Valérie Magnin[1], Tiphaine Fargetton[2], Laurent Jeannin[2], Olivier Lhote[3]

[1] Univ. Grenoble Alpes, USMB, CNRS, IRD, UGE, ISTerre, France

[2] Storengy (ENGIE), France

[3] Engie Research, ENGIE, France

Abstract

Ferroan brucite, $(Mg,Fe)(OH)_2$, is a common mineral product of serpentinization reactions. The alteration of ferroan brucite under subsurface conditions is expected to form magnetite and hydrogen (H_2). Ferroan brucite, $(Mg_{0.8}Fe_{0.2})(OH)_2$, with a grain size of 20 – 100 nm, was synthesized by precipitation of iron salts in the presence of NaOH under sub-anoxic conditions. Both composition and grain size of the synthetic product are similar to those of ferroan brucite found in serpentinized peridotites collected during the Oman Drilling Project. Synthetic ferroan brucite was then reacted in aqueous solutions at 378 and 403 K during 1 to 36 days either in PTFE-lined reactors or in gold capsules placed in externally heated pressure vessels. In gold capsules, ferroan brucite barely reacted and minor magnetite and H_2 were produced. In PTFE-lined reactors, reaction progress over 75% could be achieved with reaction products composed of magnetite, pyroaurite $[Mg_6Fe_2(OH)_{16}(CO_3)\bullet 4.5H_2O]$, and a new phase, identified as ferrian brucite $[(Mg_{0.8}Fe^{III}_{0.2})O_{0.2}(OH)_{1.8}]$ based on the Rietveld refinement of its X-ray powder diffraction data, Fe^{III}/Fe_{tot} colorimetric determination and thermogravimetric analysis. Ferrian brucite is isostructural to ferroan brucite and displays the same iron/magnesium ratio. However, all iron is trivalent. X-ray diffraction and thermogravimetric data support deprotonation as the mechanism responsible for charge compensating Fe^{II} oxidation ($Fe^{2+} + OH^- \Rightarrow Fe^{3+} + O^{2-}$). The difference in reaction products obtained with the two types of reactors is attributed to the higher permeability to H_2 (and/or O_2) of the PTFE-lined reactors compared to gold capsules. Ferroan brucite conversion into ferrian brucite was unexpectedly fast and proceeded in a few days. The thermodynamic stability of ferrian brucite is discussed as a function of oxygen fugacity and pH.

Keywords: ferroan brucite oxidation, ferrian brucite, serpentinization, low-temperature alteration, H_2 production.

1 Introduction

Seepages of natural H_2-containing gas are encountered onshore in association with ultramafic bodies that interact chemically with meteoritic waters under sub-surface conditions (Neal and Stanger 1983; Coveney et al. 1987; Abrajano et al. 1990). Petrographic investigation of Oman ophiolite samples has actually shown that the alteration under subsurface conditions of minerals bearing ferrous iron hosted in partially to fully serpentinized samples can lead to further iron oxidation, probably coupled with H_2 production (Mayhew et al. 2018; Ellison et al. 2021). Among serpentinization mineral products, ferroan brucite appears to be the most reactive in the course of low-temperature alteration processes and has thus been the subject of growing interest as a possible contributor to low temperature H_2 generation which may in turn fuel hydrogenotrophic microbial activity (Malvoisin 2015; Jöns et al. 2017; Miller et al. 2017; Klein et al. 2020; Templeton and Ellison 2020).

Brucite structure was initially determined by Aminoff (1921) and is composed of layers of edge-sharing octahedra. Subsequent investigations of structural analogues by infrared spectroscopy (Brindley and Kao 1984) and neutron diffraction (Chakoumakos et al. 1997) showed that hydroxyl groups are perpendicular to the layer. Ferroan brucite, $(Mg_{1-x}Fe^{II}_x)(OH)_2$, preserved in serpentinized peridotites contains significant divalent iron with *x* generally ranging from 0.15 to 0.4 per formula unit in samples collected at mid-ocean ridges, in ophiolites, and in forearc settings (D'Antonio and Kristensen 2004; Bach et al. 2006; Beard et al. 2009; Klein et al. 2009, 2014; Kodolányi and Pettke 2011; Kodolányi et al. 2012; Frost et al. 2013; Schwarzenbach et al. 2016; Malvoisin et al. 2020). Thermochemical models have shown that equilibrium between the $Fe(OH)_2$ component of ferroan brucite and magnetite buffers the H_2 activity (e.g., McCollom and Bach 2009) through the equilibrium:

$$3\ Fe(OH)_2 = Fe_3O_4 + H_2 + 2\ H_2O \quad (1)$$

Reaction (1) can also be used to calculate $Fe(OH)_2$ activity in brucite at a given H_2 partial pressure assuming a ferroan brucite solid-solution model and knowing the thermodynamic parameters of the $Fe(OH)_2$ end-member. Thermodynamic models involving Fe-bearing brucite that reasonably

reproduce natural observations and experimental data have been proposed (Bach and Klein 2009; Klein et al. 2009, 2013; McCollom and Bach 2009; Jöns et al. 2017). On simple thermodynamic grounds, it can be predicted that ferroan brucite initially formed by oceanic serpentinization may further produce H_2 when exposed to meteoric water. According to Reaction (1), potential change in H_2 activity will lead to the production of more magnetite (and additional H_2), thereby consuming the $Fe(OH)_2$ component of ferroan brucite. Such a change in H_2 activity may occur by dilution due to fluid infiltration, loss to the atmosphere, or consumption through microbial activity (Takai et al. 2004; Petersen et al. 2011; Myagkiy et al. 2020). This simple mechanism of H_2 production through near-surface fluid-rock interactions might be more complicated in natural systems where aqueous fluids contain dissolved species (SO_4^{2-}, Cl^-, HCO_3^-) and O_2. Oxidation of ferroan brucite may thus yield Fe^{II}/Fe^{III} layered double hydroxides containing chlorine (iowaite; Klein et al. 2020) or CO_2 (pyroaurite; Boschi et al. 2017) with or without simultaneous H_2 production.

In order to gain insight on the behavior of ferroan brucite when exposed to fluids in subsurface conditions relevant to ophiolite settings, ferroan brucite was synthesized and compared (composition, size, morphology) to natural ferroan brucite from the Oman ophiolite. Synthetic ferroan brucite was then reacted in the presence of water at temperatures close to 373 K, considered here as low temperatures. The characterization of the reaction products with X-ray diffraction, scanning electron microscopy, bulk Fe^{III} determination by colorimetry, and thermogravimetric analysis allowed us to propose phase relationships for ferroan brucite in the naturally relevant $FeO\text{-}MgO\text{-}H_2O+/\text{-}O_2$ sub-system.

2 Materials and Methods

2.1 Fe^{II}-bearing brucite synthesis

Ferroan brucite with $x \sim 0.2$ was synthesized at ambient conditions based on a method used to synthesize aqueous Fe^{II} precipitates (Olowe and Génin 1991; Gilbert et al. 2008). Ferroan brucite was

precipitated from a stoichiometric solution of dissolved Fe^{II} and Mg salts, either sulphate ($MgSO_4,7H_2O$ and $FeSO_4,7H_2O$) or chloride ($MgCl_2,6H_2O$ and $FeCl_2,4H_2O$). Precipitation occurred after pouring the metal salt solution into a NaOH solution under stirring at ~ 400 rpm. The composition of the mixture is characterized by its R ratio defined as $R = \frac{[Fe^{2+}]+[Mg^{2+}]}{[NaOH]}$. Solutions of 100 mL with salt concentrations of 0.3 mol.L^{-1} were mixed with 100 mL solutions with a NaOH concentration of either 0.75 or 6 mol.L^{-1}. This led to 200 mL solutions with $R = 0.4$ and $R = 0.05$, respectively. In order to minimize the oxidation of Fe^{II}, ultrapure water (resistivity of 18.2 MΩ.cm) was boiled under continuous N_2 bubbling prior to all experiments.

The precipitate was separated from the solution by ultra-centrifugation in an airtight bottle. The bottle was then opened in a glove box under an Ar atmosphere with a continuous measurement of O_2 level indicating concentration < 10 ppm. The glove box was systematically used in the subsequent steps requiring an inert atmosphere. The precipitate was recovered and rinsed using two different procedures: 1) vacuum enhanced filtration to collect the solid on a 0.8 µm nitrocellulose filter (AAWP filter), followed by washing three to four times with a total of ~ 50 mL degassed ultrapure water without resuspending the solid fraction; and 2) repeated cycles of centrifugation, supernatant removal, resuspension of the powder paste under manual stirring with ~ 150 mL of degassed ultrapure water. Two to four cycles were needed to reach the point where the pH did not longer decrease (10.3 – 10.7 range). This second method was mainly used in the present study due to its convenience.

2.2 Ferroan brucite reactivity experiments

A total of twenty experiments was carried out by reacting Fe-bearing brucite with an aqueous solution in two types of reactors (Table 1). Eighteen experiments were performed with synthetic ferroan brucite loaded with an aqueous solution (Table 1) into 45 mL PTFE-lined vessels (Parr 4744^{TM}). Five of these experiments (Runs #01 to #05, Table 1) were performed directly with the ferroan brucite (~ 1 g) recovered after the first centrifugation stage (see the above-described procedure 2). In this case, the starting material was thus neither rinsed nor dried and was reacted

under pressure and temperature with the solution (~ 25 g) from which this ferroan brucite precipitated (pH > 13). In all other experiments, the initial ferroan brucite used was rinsed according to one of the above-described protocols. The initial pH of the solution was measured for Runs #10, #19 and #20 and found to be close to 10 (i.e., close to the pH range measured for the last rinsing cycle, *see* previous section). The reactors were loaded and sealed in the glove box and Ar atmosphere. They were then placed in an oven regulated within 1 K. Reactivity of ferroan brucite was investigated at two temperatures: 378 and 403 K and at the water vapor pressure (0.12 and 0.27 MPa, respectively). Each experiment was stopped at a specific time ranging from 1 to 36 days (Table 1). Reactors were then opened in the glove box where the solid product was recovered. The final pH of the solution measured for eleven runs (Runs #8-16, #19, and #20) is 9.4 +/- 0.5.

Two additional experiments (#17 and #18 in Table 1) were performed by loading in the glove box about 30 mg of ferroan brucite with 100 µL of degassed ultrapure water in 2 – 3 cm long gold tubes (4.4 mm outer diameter and 4.0 mm inner diameter) welded shut at one end. The open end of the capsule was then squeezed and the capsule transferred outside the glove box for immediate welding. The Au capsule was then placed in a horizontal cold seal pressure vessel for reaction at 378 K under a water pressure of 20 MPa. The temperature was measured with a Ni-NiCr thermocouple and regulated within 1 K. At the end of the experiment, the vessel was cooled down under a compressed air stream (see Brunet and Chopin 1995 for experimental details).

2.3 Gas chromatography

H_2 gas contained in the sealed gold capsules (experiments # 17 and # 18) was recovered using the method described in Malvoisin et al. (2013). The recovered gas diluted in Ar was injected with a 250 µL gas-tight syringe in a Clarus 500 gas chromatograph (Perkin Elmer^{TM}) equipped with a polymer filled column (Restek ShinCarbon^{TM}) and a thermal conductivity detector (TCD). Argon was used as carrier gas. Each gas sample was analyzed at least three times consecutively. H_2 detection limit with the gas chromatograph setup was estimated to 10 – 100 ppm. A H_2 blank experiment was performed in a sealed gold capsule with 100 µL of degassed ultrapure water. After fifteen days at 378

K and 20 MPa, no hydrogen was detected in the blank experiment. After gas chromatography analysis, the capsules were opened in the glove box where the solid was dried for several days in the Ar atmosphere before characterization.

2.4 X-ray diffraction (XRD) and Rietveld analysis

Run products were front-loaded as randomly oriented mounts in the glove box using an air-tight holder and analyzed by X-ray diffraction (XRD) with a Bruker D8 diffractometer. XRD patterns were collected from 15 to 80° (2θ) using Cu$K\alpha$ radiation and counting times of 3 s per 0.04° step. After identification of the different mineral phases, XRD patterns were analyzed using the Rietveld technique with the BGMN software (Doebelin and Kleeberg 2015). A non-exhaustive list of independently refined parameters includes: i) the proportions of the different phases present in the samples: ferroan brucite [containing Fe^{II}], pyroaurite [a Fe-containing layered double hydroxide (LDH) structure], magnetite, and ferrian brucite [containing Fe^{III}]; ii) the unit-cell parameters of these phases; iii) the Mg:Fe ratios in ferroan and ferrian brucites if present at > 10 and >25 wt.%, respectively; iv) z-coordinate of the O atom 2d position in ferroan and ferrian brucites (space group $P\bar{3}m1$) if present at >50 wt%; v) preferred orientation of the different phases using spherical harmonic functions if the phase content was sufficient (Doebelin and Kleeberg 2015); vi) size of the coherent scattering domains and strain in the different phases. In particular, the partial occupancy of the mixed (Fe,Mg) site refined in ferroan brucite was constrained both from the variation of the in-plane *a* unit-cell parameter between values reported for $Mg(OH)_2$ (brucite – ICDD #44-1482) and $Fe(OH)_2$ (amakinite – ICSD #107289) end-members and from the influence of site mixed occupancy on the intensity distribution between *hkl* reflections. To our knowledge, no systematic study is available to confirm the validity of Vegard's law between these two end-members. The remarkably linear relationship existing between the in-plane dimension of brucite-like structures and the ionic radius of the octahedral cation ($R^2 = 0.996$ – Fig. S1) strongly supports the validity of the approach, however. Unit-cell *c* parameter was not included in the approach owing to the more erratic variation of this dimension with the ionic radius of the octahedral cation (Fig. S1). Intensity distribution between

reflections was used as an additional constraint to refine the partial occupancy of the mixed (Fe,Mg) site when proportion of ferroan brucite exceeded 10 wt.%. As no structure model was available for ferrian brucite, unit-cell parameters and Fe contents were refined independently when proportion of ferrian brucite exceeded 25 wt.% and charge compensation was hypothesized to originate either from the presence of octahedral vacancies or from the partial deprotonation of the layered structure as proposed by Genin et al. (2006a) for the octahedral layer of fully oxidized green rust. In the latter case, the partial occupancy of the mixed (Fe,Mg) site was refined using a split site and constraining a complete (Fe+Mg) site occupancy. In the former case, the Fe content was kept constant and similar to that in ferroan brucite (0.17 Fe per octahedral site) and only Mg site occupancy was refined to avoid refinement of cross-correlated parameters related to electron density at the octahedral cation position (overall site occupancy and Mg:Fe ratio).

2.5 SEM imaging

Powders of the starting material and of the run products were mounted on double-sided carbon tape in the glove box under Ar atmosphere. They were then coated under vacuum with a 1 nm thick gold layer and characterized with a field emission gun scanning electron microscope (FEG-SEM; Zeiss Ultra 55) operated at 5 to 10 kV accelerating voltage.

2.6 Thermogravimetric analysis

Thermogravimetric analyses (TGA) were performed using a Mettler-Toledo TGA-DSC3+ instrument. Samples were loaded into 100 µL aluminum crucibles inside the glove box. The crucibles were mechanically sealed in the glove box using a manual press (Mettler-Toledo) and then brought to the instrument. The lid was pierced using a small needle just prior to the measurements to minimize atmosphere exposure. A thermal treatment consisting of a 5 min isotherm at 298.15 K and a subsequent ramp from 298.15 to 873.15 K at 10 K/min was programmed, under a 50 mL/min N_2 flow. The gas produced by the sample during the TGA measurement was analyzed using an IS50 Fourier Transform Infrared (FTIR) spectrometer from Thermo Scientific. The gas was transferred from the outlet of the TGA instrument to the spectrometer using a heated transfer line (573 K). 40 scans were

acquired and averaged every 51 s. Absorbance spectra were measured from 4500 to 500 cm^{-1}, with a 4 cm^{-1} resolution.

2.7 Raman microspectroscopy

Value of *x* in the ferroan brucite was determined by Raman spectroscopy with a confocal Horiba LabRAM Soleil equipped with a 532 nm laser at ISTerre. The confocal aperture was set at 200 µm and the gratings at 600 groves/mm. Five duplicate spectra were acquired over the 3200-3800 cm^{-1} range with a x100 objective. After subtracting the baseline, spectra were fitted with Lorentzian functions to determine the position of the ν_1 O-H stretching band of ferroan brucite. This position was then used to calculate *x* using the linear relationship from Templeton and Ellison (2020).

2.8 Ferric and ferrous iron quantification in the solid products

For Runs #19 and 20, ferric and ferrous iron contents of the starting ferroan brucite and of its hydrothermal reaction products were determined by colorimetric assay with a ~ 3% precision. Sample preparation for Fe quantification was performed in a glove box under an Ar atmosphere containing 3 ppmv O_2. A mass of 103 mg of sample powder was dissolved into 4 mL of 3M HCl according to the protocol proposed in Pan et al. (2020). The resulting solution was first diluted to 50 mL with ultrapure water (18.2 MΩ) and then diluted again 10 times in ultrapure water. A 1 mL aliquot of this last solution was mixed with 1 mL of a pH-buffered solution (pH = 3.5); then, 1 mL of ultrapure degassed water and 1 mL of 10^{-2} M O-phenanthroline were successively added for [Fe^{2+}] quantification by spectrophotometric method (Herrera et al. 2007). Stability of aqueous Fe^{2+} in acidified solution (pH ~1) has been tested on 0.1 M $Fe^{II}Cl_2$ solutions prepared outside the glove box, with degassed water. No significant aqueous Fe^{2+} oxidation is expected in the time lapse (< 2 h) between dissolution and iron complexation in a glove box with 3 ppmv O_2. The procedure described above was repeated with 1 mL of hydroxylamine chloride instead of 1 mL of ultrapure degassed water to obtain $[Fe]_{total}$; [Fe^{3+}] was deduced from the difference between $[Fe]_{total}$ and [Fe^{2+}].

2.9 Comparison to a natural ferroan brucite from the Oman ophiolite

A ferroan brucite bearing sample was collected in the Wadi Tayin massif of the Samail Ophiolite during the Oman Drilling Project (sample BA4A-81-1-1-17; Kelemen et al. 2020). Sample mineralogical composition and microstructure are described in detail in Malvoisin et al. (2020, 2021). The sample consists of an extensively serpentinized dunite (serpentinization progress > 80%) containing olivine relicts surrounded by serpentine and ferroan brucite. Magnetite is rare. Malvoisin et al. (2021) have shown that serpentine occurs as ~ 1 µm wide lizardite columns perpendicular to the olivine surface. These columns are embedded in an aggregate of randomly oriented ferroan brucite grains (< 100 nm across). An *x* value of 0.2762 (95% confidence bounds of 0.2760 and 0.2765) was inferred by Malvoisin et al. (2020) for ferroan brucite composition based on the microprobe analyses of mixtures of lizardite columns and ferroan brucite grains.

3 Results

3.1 Characterization of synthetic ferroan brucite

The synthesis protocol led to ferroan brucite production as a single crystalline phase as shown by powder XRD (Fig. 1). The same results were obtained whether chloride of sulfate iron salt was used, and whether the solid products were recovered by vacuum enhanced filtration or centrifugation. Two peaks were identified in the 3200-3800 cm^{-1} range with Raman spectroscopy on sample FeBR_R0.4_Cl_11 (also used as starting material for Run #20; Fig. S2A): the broad peak at ~ 3586 cm^{-1} was attributed to ferroan brucite oxidation in air during measurement, whereas the sharp peak at ~ 3641 cm^{-1} was attributed to the ν_1 O-H stretching band of ferroan brucite. Using the relationship of Templeton and Ellison (2020), the position of this ν_1 O-H stretching band indicates a *x* value of 0.17 ± 0.05. Based on Vegard's law, refined unit-cell parameters confirmed the $x \sim 0.2$ composition (Tables S1, S2) that allows also reproducing the experimental distribution of intensities between the different *hkl* reflections. The FWHM of ferroan brucite diffraction peaks are similar for all synthetic samples and indicative of a 20 - 40 nm crystal size within the **ab** plane (Table 1). The

crystal size inferred from XRD data is close to the size of synthetic ferroan brucite platelets (50 - 100 nm across with homogeneous size distribution) observed with SEM (Fig. 2A and 2B). In this ferroan brucite, calculated (Mg,Fe)-O bond lengths (~ 2.13 Å – Table S2) are consistent with the prevalence of divalent cations in the structure. Bond valence calculated with the Valence program (Brown and Altermatt 1985; Brown 2009) and bond-valence parameters from Gagné and Hawthorne (2015) indicate that Fe^{II} atoms would receive 0.348 v.u. from each of its 6 surrounding O atoms. This ensures an almost ideal charge compensation (2.088 v.u.), whereas Mg^{II} atoms would receive 0.308 v.u. from each of the 6 surrounding O atoms. By contrast, bond valence calculated for Fe^{III} cations and a similar Fe-O bond length indicates that these cations would receive only 0.364 v.u. from surrounding O atoms, thus resulting in their strong undersaturation (2.184 v.u.). These charge compensation calculations support the prevalence of Fe^{II} over Fe^{III} in ferroan brucite.

Bulk Fe^{III} content has been determined experimentally for the two synthetic ferroan brucite used as initial material in Runs #20 and #19 (Fig. S3). In sample #20, which was prepared using the same protocol as all other syntheses, Fe^{III}/Fe_{tot} amounts to 0.08(1). Sample #19 was aged in the glove box until the product was covered with a thin pale reddish layer indicative of oxidation. In this extreme case, Fe^{III}/Fe_{tot} reaches 0.17(1) (Fig. S3). In both cases, these experimentally determined proportions of Fe^{II} and Fe^{III} further support the prevalence of Fe^{II} over Fe^{III} in ferroan brucite.

3.2 Identification and quantification of the products of ferroan brucite reaction in aqueous media at T ≤ 403 K

At 378 and 403 K, in PTFE-lined reactors, ferroan brucite was found to react significantly. Indeed, after one week of experiment, 20 – 30 wt.% of ferroan brucite have reacted at both temperatures (Table 1). For a duration of about a month, up to 80 – 90 wt.% of ferroan brucite has reacted at the two temperatures (Table 1). The two experiments performed in gold capsules yielded strikingly different results, ferroan brucite having barely reacted even after 26 d at 378 K (Table 1). In this case, only two reaction products were identified, magnetite [3.2(2) – 3.9(3) wt.%] and

pyroaurite [0.4(3) – 5.4(19) wt.%], a ferromagnesian LDH with interlayer water and carbonate anions (Allmann 1968), nominally $Fe_2Mg_6(OH)_{16}(CO_3)\bullet 4.5H_2O$.

The ferric iron content of the reaction products from PTFE-lined reactors has been experimentally determined for Experiments #19 and #20 which were specifically designed to quantify the oxidation of iron in the course of the ferroan brucite reaction. The starting material of Run #19 was purposely oxidized leading to a Fe^{III}/Fe_{tot} ratio of 0.17(1) (Fig. S3). This ratio increased to 0.92(1) after hydrothermal treatment for 32 days at 378 K (Run #19). Like for all other experiments, the starting material of Run #20 [Fe^{III}/Fe_{tot} ratio of 0.08(1)] was prepared to avoid as much as possible oxygen contamination. After hydrothermal treatment for 32 days at 378 K (Run #20) a Fe^{III}/Fe_{tot} ratio of 0.87(5) was measured in the reaction product (Fig. S3). Both experiments indicate that Fe is mainly present as Fe^{III} in reaction products of ferroan brucite.

Refinement of unit-cell parameters of ferroan brucite remaining in reaction products indicates that its Fe content (x) after reaction is similar to that of the starting material (~ 0.2). Magnetite was found in almost all run products (0.9 – 4.1 wt.%), even in experiments having lasted less than a week (Table 1). Pyroaurite was identified by XRD in all experiments but in proportions close to the detection limit (~ 0.2 – 0.3 wt.%) for Runs #04, #05 and #18 (Table 1). In all other runs, quantitative phase analysis yielded pyroaurite proportions of ~ 5 to ~ 30 wt.% depending on run duration and water-to-rock ratio. Another layered phase was present whose peak positions are similar to those of the initial ferroan brucite, although slightly shifted towards higher angles (Fig. 3B). This phase was assumed to be isostructural to ferroan brucite but with shorter unit-cell parameters, most likely as a consequence of Fe^{II} oxidation shown by the initial quick formation of pyroaurite, and will hereafter be referred to as ferrian brucite. Progressive replacement of ferroan brucite by ferrian brucite is illustrated on Fig. 3A where the time evolution of the XRD pattern of the run product is displayed. Accordingly, a satisfactory fit to the data was obtained assuming a contribution from this ferrian brucite structure (Fig. S4). SEM images (Fig. 2C) showed that ferrian brucite displayed the same habitus as starting ferroan brucite (Fig. 2A and 2B) with platelets of larger size however (~ 400 nm).

3.3 Crystal chemistry of ferrian brucite

For Run #03, in which ferrian brucite accounts for ~ 75% of the reaction products, its unit-cell parameters and atomic positions were refined to further constrain its crystal chemistry, and more especially its Fe/Mg ratio and Fe valence. Refined unit-cell parameters (a = 3.1255(5) Å, c = 4.6774(13) Å; space group $P\bar{3}m1$ – Tables S1, S3) suggest the presence of ~ 15% Fe^{III} in the ferrian structure using brucite and fully oxidized green rust ($Fe^{III}_6O_{12}H_8CO_3$) as end members for Vegard's law (a =3.1442 Å – ICDD #44-1482 – and a = 3.01 Å – Génin et al. 2006a – respectively). Validity of Vegard's law between these two end-members is supported by the extension of the linear regression between the in-plane a dimension of brucite-like structures and the ionic radius of the octahedral cations to include Fe^{III} (R^2 = 0.994 – Fig. S5). Validity of Vegard's law for the in-plane a parameter of mixed (Fe^{III},Mg^{II}) octahedral layers is further supported by the consistency between calculated and experimentally measured a unit-cell parameters of (Fe^{III},Mg^{II})-LDHs of similar layer composition. The a parameter calculated by Elmoubarki et al. (2017) for a LDH [$Fe^{III}_{0.27}Mg^{II}_{0.73}(OH)_2$ – 3.108 Å] is indeed equivalent to their experimentally determined value of 3.11 Å, and similar to the 3.109 Å a unit-cell parameter of pyroaurite ($Fe^{III}_{0.25}Mg^{II}_{0.75}(OH)_2$ – ICDD #1-70-2150). In addition, the Fe content refined independently for ferrian brucite from intensity distribution of its *hkl* reflections is ~ 0.17, a content similar to that of the initial brucite suggesting that all / most of ferroan brucite initial Fe^{II} was oxidized to Fe^{III}. The complete oxidation of Fe in ferrian brucite is supported further by the consistency of Fe^{III}/Fe_{tot} ratios determined experimentally and calculated from quantitative phase analysis for Runs #19 and #20 (Fig. S3 and Table S4, respectively). In addition, evolution of layer O atomic coordinate (Table S3) and of in-plane unit-cell parameters in ferrian brucite compared to ferroan brucite led to a significant shortening of the (Mg,Fe)-O bond length from ~ 2.13 Å in the initial ferroan brucite to ~ 2.08 Å in ferrian brucite. The resulting increase in the Fe-O bond valence calculated for Fe^{III}-O in ferrian brucite (0.418 v.u.) compared to Fe^{II}-O in ferroan brucite (0.348 v.u.) is consistent with the sole presence of Fe^{III} in ferrian brucite (Fe^{III} receives 2.508 v.u. from the 6

surrounding O atoms), especially as Mg remains the dominant cation (~80%) in ferrian brucite, thus preventing shortening further the average (Mg,Fe)-O bond length.

In this model, compensation of the increased positive charge induced by Fe^{II} oxidation was assumed to be achieved by partial deprotonation of the structure, as proposed by Genin et al. (2006a) for oxidized green rust, leading to a $(Fe^{III}_{y}Mg_{1-y})(OH_{(1-y/2)})_2$ structural formula. Another alternative for charge compensation is the creation of Mg octahedral vacancies. This alternative structure model was assessed for ferrian brucite by refining the partial occupancy of a mixed $[Fe_{0.17}Mg_w]$ octahedral site for Run #03. The refined $[Fe_{0.17}Mg_{0.80(2)}]$ average cationic composition of this site is ~ 1.0 and supports the absence of octahedral vacancies. This alternative model was thus rejected and it was concluded that deprotonation charge-compensates Fe^{II} oxidation in the initial ferroan brucite.

3.4 Thermogravimetric analysis of ferroan brucite and ferrian brucite rich samples

Evolution of sample mass as a function of temperature measured by TGA and its derivative are displayed in Fig. 4 for ferroan brucite (synthesized from chloride salts) and for Runs #09 and #15 which both contained over 30 wt.% ferrian brucite (Table 1). Ferroan brucite exhibits two mass loss events. The first one occurred below 461 K (Fig. 4A) which is interpreted as departure of physisorbed water (6.2 wt.%), whereas a second mass loss of much higher amplitude occurred between 500 and 700 K and is interpreted as dehydroxylation of ferroan brucite (Reaction 2):

$$(Mg,Fe)(OH)_2 = (Mg,Fe)O + H_2O \quad (2)$$

This temperature range of dehydroxylation is consistent with thermogravimetric data on synthetic brucite, $Mg(OH)_2$, which was found to dehydroxylate in the 550 – 700 K range (Turner et al. 1963; Klein et al. 2020).

In comparison, TGA analysis of reaction products shows a more limited mass loss (2.9 wt.%) due to physisorbed water that may be related to the larger grain size (smaller surface area). An additional mass loss (2.3 wt.%) is observed from 461 – 505 K (Fig. 4B and 4C). It is most likely related to the dehydration of pyroaurite interlayers that contain H_2O in addition to CO_3^{2-} anions.

Indeed, based on 4.5 H_2O per formula unit, pyroaurite structural water represents 2.9 wt.% of the total TGA weight loss (Run #15, calculated with 24.3 wt.% pyroaurite as given by Rietveld refinement). In the reaction products, the main mass loss event was found to shift towards higher temperature when the ferrian brucite content in the sample increased, from 660 K for the ferroan brucite starting material up to 692 K for Run #15 (Fig. 4D). This event is expected to include the dehydroxylation of both ferrian brucite / pyroaurite and of residual ferroan brucite. Dehydroxylation of pyroaurite and ferrian brucite are expected to occur in the same temperature range since they have identical octahedral layer composition. Coupled infrared spectroscopy indicated that CO_2 from pyroaurite was also mostly released over this temperature range. The increase in the temperature of the main mass loss event with respect to single-phase ferroan brucite could be related either to a grain size effect with ferrian brucite and pyroaurite having larger grain size than starting $(Mg_{0.8}Fe_{0.2})(OH)_2$ and/or to the valence modification in the octahedral layer due to the presence of trivalent Fe.

3.5 Natural ferroan brucite from Oman

Powder diffraction patterns and Raman spectroscopy of natural serpentinite sample show the presence of ferroan brucite and serpentine (Fig. 1B and S2B – Wadi Tayin massif, Samail ophiolite). Ferrian brucite was not detected. The comparison between the powder diffraction patterns of the synthetic product and that of ferroan brucite from the natural serpentinite sample shows that the lattice parameters are the same and that diffraction peak widths are similar, indicative of crystallite sizes in the order of 30 to 100 nm in the **ab** plane. Raman spectroscopy in the 3200-3800 cm^{-1} range on the natural sample reveals peaks similar to those observed for synthetic ferroan brucite but slightly shifted at ~ 3594 cm^{-1} for the broad peak and at ~ 3632 cm^{-1} for the sharp peak (ν_1 O-H stretching band; Fig. S2B). Using the relationship of Templeton and Ellison (2020), the position of this ν_1 O-H stretching band indicates a *x* value of 0.287 ± 0.03. This latter value is consistent with results from electron microprobe analysis on the same sample yielding x = 0.276 (Malvoisin et al. 2020). SEM characterization of both sample types confirmed the grain size derived from XRD data analysis.

4 Discussion

4.1 Magnetite and H_2 formation

When reacted in gold capsules that are known to be impermeable to H_2 below 623 K (Chou 1986), synthetic ferroan brucite only barely reacted and the identified run products were magnetite (3.2(2) - 3.9(3) wt.% – Table 1), pyroaurite, and H_2. The amount of H_2 gas produced during Runs #17 and #18 ranged from 2.87 ± 0.46 to 8.49 ± 1.5 nanomoles leading to [H_2,aq] comprised between 28.7 ± 4.6 and 84.9 ± 15 µmol/L at 20 MPa and 378 K. This amount of H_2 recovered is three orders of magnitude lower than expected if all the magnetite in the run products would have formed from ferroan brucite oxidation according to the following equation:

$$[Fe^{2+}]^{brucite} + H_2O = Fe^{3+} + OH^- + ½\ H_2 \qquad (3)$$

Based on the magnetite content of Runs #19 and #20, for which the Fe^{III} content of the starting ferroan-brucite material was analyzed, it can thus be concluded that magnetite mainly derived from trivalent iron present in the starting material (~ 10% of Fe_{tot}).

4.2 Ferroan brucite oxidation to ferrian brucite and pyroaurite

The reaction of ferroan brucite in PTFE reactors mostly involved Fe^{II} oxidation to Fe^{III} and the formation of ferrian brucite. As for the above experiments in sealed gold capsules (Runs #17 and #18), ~ 3 - 4 wt.% of magnetite has formed, most likely from Fe^{III} present in the starting material (and O_2 contamination). This Fe^{III} did not form hematite that could have been produced if more oxidizing conditions had prevailed in the experimental setup. Similarly, lepidocrocite or goethite that are easily formed in air from $Fe(OH)_2$ (Olowe and Génin 1991; Gilbert et al. 2008) were not detected.

The formation of ferrian brucite in PTFE reactor and its absence in experiments performed in gold capsules at the same temperature, duration and absence of stirring, can be interpreted as reflecting different RedOx conditions in the two setups. Whereas gold capsules are not permeable to H_2 at the temperatures of the present experiments (378 – 403 K), PTFE reactors with a PTFE seal are known to be more permeable to gases, and even to store gases in the PTFE macro-porosity (Vacher

et al. 2019). In PTFE reactors where significant outward H_2 diffusion and/or inward O_2 diffusion cannot be avoided, RedOx conditions occurred to be favorable to the oxidation of Fe^{II} contained in ferroan brucite layer to form ferrian brucite.

At 378 K, the ferroan brucite transformation to ferrian brucite seemed to follow zero-order kinetics irrespective of the reaction medium, i.e., ultrapure degassed water or ferroan brucite synthesis solution (Fig. 5). Magnetite and pyroaurite formed before ferrian brucite in the early stage of the experiments in both aqueous media. Departure from zero-order kinetics of the ferroan-to-ferrian brucite transformation in the first 3 days of experiments may thus be interpreted as the result of rapid pyroaurite (and possibly magnetite) formation. This early transformation of ferroan brucite can be considered as fast since it proceeded at the day scale at temperatures relevant to subsurface conditions.

The amount of pyroaurite product appears to be proportional to the water-to-rock ratio indicating that the main source of CO_2 is likely the CO_2 dissolved in the added solution (Table 1). Indeed, CO_2 is highly soluble at elevated pH in NaOH solutions (Yoo et al. 2013 and references therein). This strong partitioning of CO_2 into pyroaurite confirms the potential of this mineral as efficient CO_2 sink in rocks or mine tailing containing Fe-brucite (e.g., Assima et al. 2014; Boschi et al. 2017; Turvey et al. 2018). The low concentration (~ 2 wt.%) or even the absence of pyroaurite in experiments performed in sealed gold-capsule where the highest H_2 pressure has been attained might result from a combination of low water-to-rock ratio and of reducing conditions that hindered or prevented the oxidation of Fe^{II} to Fe^{III} in ferroan brucite and the associated formation of pyroaurite $(Fe^{III},Mg)(OH)_2$ octahedral layer.

4.3 Transformation mechanisms of ferroan brucite into ferrian brucite

The similarity between initial ferroan brucite and ferrian brucite product in terms of constitutive crystallite sizes, suggests that changes affecting the octahedral layer remained limited to Fe^{II} oxidation and to the induced partial deprotonation to compensate for the increased cationic charge. This similarity and similar Fe/Mg ratios determined in ferroan and ferrian brucites both indicate an isomorphic oxidation process. Rietveld refinement of ferrian brucite indicated little or no

octahedral vacancies, thus supporting deprotonation of the hydroxyl groups ($Fe^{2+}+ OH^- = Fe^{3+} + O^{2-}$) as the mechanism balancing the charge resulting from Fe^{II} oxidation in brucite octahedral layers.

Based on the phase proportions and their estimated standard deviations (esd) derived from Rietveld refinement and considering the following nominal compositions, $(Mg_{0.81}Fe^{II}_{0.19})(OH)_2$, $(Mg_{0.83}Fe^{III}_{0.17})O_{0.17}(OH)_{1.83}$ and $Mg_6Fe^{III}_2(CO_3)(OH)_{16}.4.5H_2O$ for ferroan brucite, ferrian brucite and pyroaurite, respectively, a theoretical total mass loss (H_2O and CO_2) of 28.9(8) wt.% was calculated for Run #15. This prediction agrees well with the experimental total mass loss of Run #15 which amounts to 27.2(2) wt.% after subtraction of the contribution of physisorbed water. For comparison, the alternative model which considers a ferrian brucite composition with octahedral vacancies, $(Mg_{0.76}\square_{0.08}Fe^{III}_{0.16})(OH)_2$, would lead to a total mass loss of 30.6(8) wt.%. TGA data thus support further the deprotonation model to charge balance the presence of Fe^{III} in the octahedral sheets of ferrian brucite consistent with the Rietveld refinement of XRD data. The equation to describe the oxidation of ferroan brucite is thus most likely:

$$(Mg_{0.8},Fe^{II}_{0.2})(OH)_2 \Rightarrow (Mg_{0.8},Fe^{III}_{0.2})O_{0.2}(OH)_{1.8} + 0.1\ H_2 \quad (4)$$

In the same chemical system, fougerite which belongs to the green rust mineral group also possesses a structure based on brucite-like octahedral sheets with interlayer water molecules and anion(s). The structural formula of fougerite is $[Fe^{II}_{1-z}Fe^{III}_z\ Mg_y(OH)_{2+2y}]^{+z}\ [z/nA^{-n}.mH_2O]^{-z}$ where *A* is the interlayer anion (OH^-, Cl^-, CO_3^{2-}, SO_4^{2-}) and *n* its valency (Trolard et al. 2007). The charge excess of the octahedral sheet is compensated for by the presence of interlayer anions. Génin et al. (2006b) consistently showed that the oxidation of synthetic (CO_3^{2-}) green rust can be achieved following the general substitution scheme $Fe^{II}_{6(1-z)}Fe^{III}_{6z}O_{12}H_{2(7-3z)}CO_3$ which involves charge compensation by progressive deprotonation.

5 Implications

5.1 Ferrian brucite stability in the FeO-MgO-H_2O+/-O_2 system

The oxidation of $Fe(OH)_2$ in air (high oxygen fugacity; fO_2) produces goethite, lepidocrocite, or hematite (α-FeOOH, γ-FeOOH, and α-Fe_2O_3, respectively; Gilbert et al. 2008). The experiments in gold capsules performed at 378 K confirmed that under low fO_2 conditions, H_2 is produced during ferroan brucite oxidation. Under these conditions, the only oxidized reaction product was magnetite, suggesting that reaction (1) led to H_2 production, even though the presence of trivalent iron in the starting material also significantly contributed to magnetite formation (Ellison et al. 2021; Mayhew et al. 2013; Miller et al. 2017). In the PTFE reactors, ferrian brucite was formed and the fO_2 was thus intermediate between that of sealed gold capsules and air (intermediate fO_2). It cannot be concluded at this stage whether ferrian brucite was a stable or a metastable phase. It can however be deduced from its coexistence with magnetite observed in PTFE experiments that its stability/metastability field should fall in a fO_2 range comprised between the stability fields of ferroan brucite and of hematite. To confirm this statement, the thermodynamic properties of ferrian brucite, $(Mg_{1-x},Fe^{III}_x)O_x(OH)_{2-x}$, were computed from a linear combination of the thermodynamic properties of goethite and brucite with the slop16.dat database (Fig. 6). Obviously, such an approximation is fraught with uncertainty. The effect of changing the Gibbs energy of formation ($\Delta G°_f$) of ferrian brucite in the calculation by ± 10 kJ/mol was thus considered. Within that range of $\Delta G°_f$, the topology remains unchanged and ferrian brucite is always found to occur at fO_2 comprised between those of ferroan brucite and hematite stability fields (Fig. 6). However, the uncertainty on the thermodynamic parameters does not allow to determine if O_2 or H_2 is the dominant gas species in the stability field of ferrian brucite (Fig. 6). It is thus still unclear whether ferrian brucite formed in PTFE-lined reactors at the expense of ferroan brucite by consuming O_2 or by producing H_2, according to one of the following reactions:

$$(Mg_{0.8},Fe^{II}_{0.2})(OH)_2 + 0.05\ O_2 = (Mg_{0.8},Fe^{III}_{0.2})O_{0.2}(OH)_{1.8} + 0.1\ H_2O \quad (5)$$

or

$$(Mg_{0.8},Fe^{II}_{0.2})(OH)_2 = (Mg_{0.8},Fe^{III}_{0.2})O_{0.2}(OH)_{1.8} + 0.1\ H_2 \quad (6)$$

One should note that Tosca et al. (2008) observed H_2 production during $Fe(OH)_2$ conversion into green rust-CO_3, which, as shown above, shares crystallographic properties with ferrian brucite. Additional experiments in the FeO-MgO-H_2O+/-O_2 system are still needed to constrain the exact range of fO_2-T conditions under which ferrian brucite may be expected to occur in nature.

5.2 Ferroan brucite oxidation kinetics

Mineral replacement reactions generally proceed through dissolution and precipitation which are mineral-surface dependent leading to non-constant replacement rates (Putnis 2002; Malvoisin et al. 2012). The conversion from ferroan to ferrian brucite appeared here to follow zero-order kinetics, indicating that reaction rate is not controlled by this common dissolution-precipitation process. The fact that ferrian brucite is likely stable at relatively low H_2 partial pressure (Fig. 6) implies that Reaction (6) cannot reach large extent in closed system. H_2 partial pressure should indeed remain low to maintain the system in the stability field of ferrian brucite. Large reaction extents as those observed here (e.g., > 75%) would thus require extraction of at least part of the H_2 produced according to Reaction (6). As a result, ferroan to ferrian brucite conversion was likely controlled by the rate of H_2 permeation through the PTFE reactor. This latter rate is expected to be constant (and the reaction kinetics of zero order) if H_2 permeates into an infinite gas reservoir, which is a reasonable approximation for the room in which the experiments were conducted. A symmetrical scenario involving atmospheric O_2 permeation into the reactor would yield similar results and cannot be ruled out at this stage to account for ferrian brucite formation.

This being said, ferroan brucite oxidation into ferrian brucite and/or pyroaurite revealed to be remarkably fast even at temperatures as low as 378 K. Indeed, about half of the starting ferroan brucite converted into ferrian brucite after 15 days and more than 90% reacted after 36 days (Table 1). Ferrian brucite and pyroaurite (like other LDH containing different anions) are based on the same structural arrangement composed of brucite-like octahedral layers. They actually differ only in the way octahedral Fe^{III} is charge balanced: incorporation of an interlayer anion (CO_3^{2-}, Cl^-, SO_4^{2-}) group or partial deprotonation of the brucite-like layer, respectively. The fact that these two charge-balance

mechanisms do not involve recrystallization of the octahedral layer might explain why they are effective at a temperature as low as 378 K and on a day – week timescale (Fig. 5).

Although ferrian brucite may well no be a stable phase in the FeO-MgO-H_2O+/-O_2 system, the relatively fast transformation of ferroan into ferrian brucite makes the latter a likely metastable state in the ferroan brucite reaction process into Fe(III)-bearing oxides/hydroxides according to Ostwald's rule of stages. It must be noted that deprotonation coupled to iron oxidation in brucite layers is also relevant to clay minerals such as smectite (Drits and Manceau 2000; Manceau et al. 2000). Interestingly, this process was found to occur in soils at a relative short timescale of several months.

5.3 Why ferrian brucite has never been reported in ophiolites?

The reddish color and chemical analyses of brucite in some natural samples indicate ferroan brucite oxidation (Beard and Hopkinson 2000; Beard and Frost 2016; Ellison et al. 2021). However, the presence of ferrian brucite was not confirmed by mineralogical analysis and ferric (oxyhydr)oxides could lead to the same characteristics. The ubiquitous presence of anions in natural fluids (e.g., seawater, meteoric waters) likely favors the formation of green rust group minerals over that of ferrian brucite. In addition to pyroaurite discussed above, iowaite ($Mg_6Fe^{III}_2Cl_2(OH)_{16}.4H_2O$; Kohls and Rodda 1967) is another LDH reported in serpentinized peridotites (Heling and Schwarz 1992; Gibson et al. 1996; Bach et al. 2004; D'Antonio and Kristensen 2004; Sharp and Barnes 2004; Moll et al. 2007; Bonifacie et al. 2008; Kodolányi and Pettke 2011; Kodolányi et al. 2012; Albers et al. 2020). It occurs in samples collected at mid-ocean ridges, on passive margins and in ophiolites where it is generally associated at the submicrometer scale with ferroan brucite (Klein et al. 2020). Heling and Schwarz (1992) proposed that iowaite forms from brucite with iron oxidation charge-balanced by interlayer Cl^-. This reaction is thought to occur under the oxidizing conditions associated to weathering at low temperature (Bach et al. 2004). However, methane was reported in seamounts where iowaite was found (Heling and Schwarz 1992), suggesting that iowaite formation, similarly to ferrian brucite formation in the experiments reported here, does not necessarily involve oxidizing

conditions. Similarly, Génin et al. (2006b) and Ruby et al. (2010) determined Eh-pH diagrams in which naturally occurring green rust group minerals (mixed valence Fe^{II},Fe^{III} LDHs) are stable in the same field as molecular hydrogen.

Funding sources

This work was funded by ENGIE – France. This research did not receive any specific grant from funding agencies in the public or not-for-profit sectors.

CRediT authorship contribution statement

William Carlin: Methodology, Investigation, Data Curation, Writing – Original Draft, Visualization. **Benjamin Malvoisin:** Conceptualization, Formal analysis, Writing – Original Draft, Writing – Review & Editing, Supervision, Visualization. **Bruno Lanson:** Methodology, Software, Investigation, Writing – Review & Editing, Visualization. **Fabrice Brunet:** Conceptualization, Formal analysis, Writing – Original Draft, Writing – Review & Editing, Supervision. **Nathaniel Findling:** Methodology, Software. **Martine Lanson:** Methodology, Investigation. **Valérie Magnin:** Investigation. **Tiphaine Fargetton:** Review and Supervision. **Laurent Jeannin:** Review and Supervision. **Olivier Lhote:** Project administration.

Declaration of Competing Interest

The authors declare no known competing financial interests or personal relationships that could have appeared to influence the work reported in this article.

Data availability

The data presented in this study are available on request from the corresponding author.

Acknowledgements

The authors thank Alejandro Fernandez-Martinez (ISTerre) for his help with the TGA device and Thibault Rondet (ISTerre) for his preliminary work on ferroan brucite synthesis. Samples and data described in the present article were obtained and analyzed using the Geochemistry-Mineralogy platform of ISTerre (Grenoble). The authors are grateful for the comments of C. Ruby, C. Turvey and E. Ellison on an earlier version of the manuscript.

References

Abrajano, T.A., Sturchio, N.C., Kennedy, B.M., Lyon, G.L., Muehlenbachs, K., Bohlke, J.K., 1990. Geochemistry of reduced gas related to serpentinization of the Zambales ophiolite, Philippines. Appl. Geochem. 5, 625–630. https://doi.org/10.1016/0883-2927(90)90060-I

Albers, E., Kahl, W.-A., Beyer, L., Bach, W., 2020. Variant across-forearc compositions of slab-fluids recorded by serpentinites: Implications on the mobilization of FMEs from an active subduction zone (Mariana forearc). Lithos 364–365, 105525. https://doi.org/10.1016/j.lithos.2020.105525

Allmann, R., 1968. The crystal structure of pyroaurite. Acta Crystallogr. B 24, 972–977. https://doi.org/10.1107/S0567740868003511

Aminoff, G., 1921. XXV. Über die Struktur des Magnesiumhydroxydes. Z. Krist.-Cryst. Mater. 56, 506–509. https://doi.org/10.1524/zkri.1921.56.1.506

Assima, G.P., Larachi, F., Molson, J., Beaudoin, G., 2014. Comparative study of five Québec ultramafic mining residues for use in direct ambient carbon dioxide mineral sequestration. Chem. Eng. J. 245, 56–64. https://doi.org/10.1016/j.cej.2014.02.010

Bach, W., Garrido, C.J., Paulick, H., Harvey, J., Rosner, M., 2004. Seawater-peridotite interactions: First insights from ODP Leg 209, MAR 15°N. Geochem. Geophys. Geosyst. 5. https://doi.org/10.1029/2004GC000744

Bach, W., Klein, F., 2009. The petrology of seafloor rodingites: Insights from geochemical reaction path modeling. Lithos 112, 103–117. https://doi.org/10.1016/j.lithos.2008.10.022

Bach, W., Paulick, H., Garrido, C.J., Ildefonse, B., Meurer, W.P., Humphris, S.E., 2006. Unraveling the sequence of serpentinization reactions: petrography, mineral chemistry, and petrophysics of serpentinites from MAR 15°N (ODP Leg 209, Site 1274). Geophys. Res. Lett. 33, L13306. https://doi.org/10.1029/2006GL025681

Beard, J.S., Frost, B.R., 2016. The stoichiometric effects of ferric iron substitutions in serpentine from microprobe data. Int. Geol. Rev. 59, 541–547. https://doi.org/10.1080/00206814.2016.1197803

Beard, J.S., Frost, B.R., Fryer, P., McCaig, A., Searle, R., Ildefonse, B., Zinin, P., Sharma, S.K., 2009. Onset and progression of serpentinization and magnetite formation in olivine-rich troctolite from IODP Hole U1309D. J. Petrol. 50, 387–403. https://doi.org/10.1093/petrology/egp004

Beard, J.S., Hopkinson, L., 2000. A fossil, serpentinization-related hydrothermal vent, Ocean Drilling Program Leg 173, Site 1068 (Iberia abyssal plain): Some aspects of mineral and fluid chemistry. J. Geophys. Res. 105, 16527–16539. https://doi.org/10.1029/2000JB900073

Bonifacie, M., Busigny, V., Mével, C., Philippot, P., Agrinier, P., Jendrzejewski, N., Scambelluri, M., Javoy, M., 2008. Chlorine isotopic composition in seafloor serpentinites and high-pressure metaperidotites. Insights into oceanic serpentinization and subduction processes. Geochim. Cosmochim. Ac. 72, 126–139. https://doi.org/10.1016/j.gca.2007.10.010

Boschi, C., Dini, A., Baneschi, I., Bedini, F., Perchiazzi, N., Cavallo, A., 2017. Brucite-driven CO2 uptake in serpentinized dunites (Ligurian Ophiolites, Montecastelli, Tuscany). Lithos 288–289, 264–281. https://doi.org/10.1016/j.lithos.2017.07.005

586 Brindley, G.W., Kao, C.-C., 1984. Structural and IR relations among brucite-like divalent metal
587 hydroxides. Phys. Chem. Miner. 10, 187–191. https://doi.org/10.1007/BF00311476

588 Brown, I.D., 2009. Recent developments in the methods and applications of the bond valence model.
589 Chem. Rev. 109, 6858–6919. https://doi.org/10.1021/cr900053k

590 Brown, I.D., Altermatt, D., 1985. Bond-valence parameters obtained from a systematic analysis of
591 the Inorganic Crystal Structure Database. Acta Crystallogr. B 41, 244–247.
592 https://doi.org/10.1107/S0108768185002063

593 Brunet, F., Chopin, C., 1995. Bearthite, $Ca_2Al(PO_4)_2OH$: stability, thermodynamic properties and
594 phase relations. Contr. Mineral. Petrol. 121, 258–266. https://doi.org/10.1007/BF02688241

595 Chakoumakos, B.C., Loong, C.-K., Schultz, A.J., 1997. Low-Temperature Structure and Dynamics
596 of Brucite. J. Phys. Chem. B 101, 9458–9462. https://doi.org/10.1021/jp972225a

597 Chou, I.-M., 1986. Permeability of precious metals to hydrogen at 2kb total pressure and elevated
598 temperatures. Am J Sci 286, 638–658. https://doi.org/10.2475/ajs.286.8.638

599 Coveney, R., Goebel, E., Zeller, E., Dreschhoff, G., Angino, E., 1987. Serpentinization and the origin
600 of hydrogen gas in Kansas. AAPG Bull. 71, 39–48. https://doi.org/10.1306/94886D3F-1704-
601 11D7-8645000102C1865D

602 D'Antonio, M., Kristensen, M.B., 2004. Serpentine and brucite of ultramafic clasts from the South
603 Chamorro Seamount (Ocean Drilling Program Leg 195, Site 1200): inferences for the
604 serpentinization of the Mariana forearc mantle. Mineral. Mag. 68, 887–904.
605 https://doi.org/10.1180/0026461046860229

606 de Obeso, J.C., Kelemen, P.B., 2020. Major element mobility during serpentinization, oxidation and
607 weathering of mantle peridotite at low temperatures. Phil. Trans. R. Soc. A 378, 20180433.
608 https://doi.org/10.1098/rsta.2018.0433

609 Doebelin, N., Kleeberg, R., 2015. Profex : a graphical user interface for the Rietveld refinement
610 program BGMN. J. Appl. Crystallogr. 48, 1573–1580.
611 https://doi.org/10.1107/S1600576715014685

612 Drits, V.A., Manceau, A., 2000. A model for the mechanism of Fe^{3+} to Fe^{2+} reduction in dioctahedral
613 smectites. Clay Clay Miner. 48, 185–195. https://doi.org/10.1346/CCMN.2000.0480204

614 Ellison, E.T., Templeton, A.S., Zeigler, S.D., Mayhew, L.E., Kelemen, P.B., Matter, J.M., The Oman
615 Drilling Project Science Party, 2021. Low- temperature hydrogen formation during aqueous
616 alteration of serpentinized peridotite in the Samail ophiolite. J. Geophys. Res. Solid Earth 126.
617 https://doi.org/10.1029/2021JB021981

618 Elmoubarki, R., Mahjoubi, F.Z., Elhalil, A., Tounsadi, H., Abdennouri, M., Sadiq, M., Qourzal, S.,
619 Zouhri, A., Barka, N., 2017. Ni/Fe and Mg/Fe layered double hydroxides and their calcined
620 derivatives: preparation, characterization and application on textile dyes removal. J. Mater.
621 Res. Technol. 6, 271–283. https://doi.org/10.1016/j.jmrt.2016.09.007

622 Frost, B.R., Evans, K.A., Swapp, S.M., Beard, J.S., Mothersole, F.E., 2013. The process of
623 serpentinization in dunite from New Caledonia. Lithos 178, 24–39.
624 https://doi.org/10.1016/j.lithos.2013.02.002

Gagné, O.C., Hawthorne, F.C., 2015. Comprehensive derivation of bond-valence parameters for ion pairs involving oxygen. Acta Crystallogr. B 71, 562–578. https://doi.org/10.1107/S2052520615016297

Génin, J.-M.R., Ruby, C., Upadhyay, C., 2006a. Structure and thermodynamics of ferrous, stoichiometric and ferric oxyhydroxycarbonate green rusts; redox flexibility and fougerite mineral. Solid State Sci. 8, 1330–1343. https://doi.org/10.1016/j.solidstatesciences.2006.05.010

Génin, J.-M.R., Ruby, C., Géhin, A., Refait, P., 2006b. Synthesis of green rusts by oxidation of $Fe(OH)_2$, their products of oxidation and reduction of ferric oxyhydroxides; –pH Pourbaix diagrams. C. R. Geosci. 338, 433–446. https://doi.org/10.1016/j.crte.2006.04.004

Gibson, I.L., Beslier, M.O., Cornen, G., Milliken, K.L., Seifert, K.E., 1996. Major-and trace-element seawater alteration profiles in serpentinite formed during the development of the Iberia Margin, Site 897. Proceedings-Ocean Drilling Program Scientific Results 149, 519–528.

Gilbert, F., Refait, P., Lévêque, F., Remazeilles, C., Conforto, E., 2008. Synthesis of goethite from $Fe(OH)_2$ precipitates: Influence of Fe(II) concentration and stirring speed. J. Phys. Chem. Solids 69, 2124–2130. https://doi.org/10.1016/j.jpcs.2008.03.010

Heling, D., Schwarz, A., 1992. Iowaite in serpentinite muds at Sites 778, 779, 780, and 784: a possible cause for the low chlorinity of pore waters, in: Proc. Ocean Drill. Prog., Sci. Results 125, 313–323. https://doi.org/10.2973/odp.proc.sr.125.176.1992

Herrera, L., Ruiz, P., Aguillon, J.C., Fehrmann, A., 2007. A new spectrophotometric method for the determination of ferrous iron in the presence of ferric iron. J. Chem. Technol. Biotechnol. 44, 171–181. https://doi.org/10.1002/jctb.280440302

Jöns, N., Kahl, W.-A., Bach, W., 2017. Reaction-induced porosity and onset of low-temperature carbonation in abyssal peridotites: Insights from 3D high-resolution microtomography. Lithos 268–271, 274–284. https://doi.org/10.1016/j.lithos.2016.11.014

Kelemen, P.B., Matter, J.M., Teagle, D.A.H., Coggon, J.A., Oman Drilling Science Team, 2020. Oman Drilling Project: Scientific Drilling in the Samail Ophiolite, Sultanate of Oman. Proceedings of the Oman Drilling Project. https://doi .org /10 .14379 /OmanDP.proc .2020.

Klein, F., Bach, W., Humphris, S.E., Kahl, W.-A., Jons, N., Moskowitz, B., Berquo, T.S., 2014. Magnetite in seafloor serpentinite--Some like it hot. Geology 42, 135–138. https://doi.org/10.1130/G35068.1

Klein, F., Bach, W., Jöns, N., McCollom, T., Moskowitz, B., Berquó, T., 2009. Iron partitioning and hydrogen generation during serpentinization of abyssal peridotites from 15°N on the Mid-Atlantic ridge. Geochim. Cosmochim. Ac. 73, 6868–6893. https://doi.org/10.1016/j.gca.2009.08.021

Klein, F., Bach, W., McCollom, T.M., 2013. Compositional controls on hydrogen generation during serpentinization of ultramafic rocks. Lithos 178, 55–69. https://doi.org/10.1016/j.lithos.2013.03.008

Klein, F., Humphris, S.E., Bach, W., 2020. Brucite formation and dissolution in oceanic serpentinite. Geochem. Persp. Lett. 1–5. https://doi.org/10.7185/geochemlet.2035

Kodolányi, J., Pettke, T., 2011. Loss of trace elements from serpentinites during fluid-assisted transformation of chrysotile to antigorite — An example from Guatemala. Chem. Geol. 284, 351–362. https://doi.org/10.1016/j.chemgeo.2011.03.016

Kodolányi, J., Pettke, T., Spandler, C., Kamber, B.S., Gméling, K., 2012. Geochemistry of ocean floor and fore-arc serpentinites: constraints on the ultramafic input to subduction zones. J. Petrol. 53, 235–270. https://doi.org/10.1093/petrology/egr058

Kohls, D.W., Rodda, J.L., 1967. Iowaite, a new hydrous magnesium hydroxide-ferric oxychloride from the Precambrian of Iowa. Am. Mineral. 52, 1261–1271.

Malvoisin, B., 2015. Mass transfer in the oceanic lithosphere: Serpentinization is not isochemical. Earth Planet. Sc. Lett. 430, 75–85. https://doi.org/10.1016/j.epsl.2015.07.043

Malvoisin, B., Auzende, A.-L., Kelemen, P.B., 2021. Nanostructure of serpentinisation products: Importance for water transport and low-temperature alteration. Earth Planet. Sc. Lett. 576, 117212. https://doi.org/10.1016/j.epsl.2021.117212

Malvoisin, B., Brunet, F., Carlut, J., Montes-Hernandez, G., Findling, N., Lanson, M., Vidal, O., Bottero, J.-Y., Goffé, B., 2013. High-purity hydrogen gas from the reaction between BOF steel slag and water in the 473–673 K range. Int. J. Hydrogen Energ. 38, 7382–7393. https://doi.org/10.1016/j.ijhydene.2013.03.163

Malvoisin, B., Brunet, F., Carlut, J., Rouméjon, S., Cannat, M., 2012. Serpentinization of oceanic peridotites: 2. Kinetics and processes of San Carlos olivine hydrothermal alteration. J. Geophys. Res. 117. https://doi.org/10.1029/2011JB008842

Malvoisin, B., Zhang, C., Müntener, O., Baumgartner, L.P., Kelemen, P.B., Oman Drilling Project Science Party, 2020. Measurement of volume change and mass transfer during serpentinization: insights from the Oman drilling project. J. Geophys. Res. Solid Earth 125. https://doi.org/10.1029/2019JB018877

Manceau, A., Lanson, B., Drits, V.A., Chateigner, D., Gates, W.P., Wu, J., Huo, D., Stucki, J.W., 2000. Oxidation-reduction mechanism of iron in dioctahedral smectites: I. Crystal chemistry of oxidized reference nontronites. Am. Mineral. 85, 133–152. https://doi.org/10.2138/am-2000-0114

Mayhew, L.E., Ellison, E.T., Miller, H.M., Kelemen, P.B., Templeton, A.S., 2018. Iron transformations during low temperature alteration of variably serpentinized rocks from the Samail ophiolite, Oman. Geochim. Cosmochim. Ac. 222, 704–728, https://doi.org/10.1016/j.gca.2017.11.023.

McCollom, T.M., Bach, W., 2009. Thermodynamic constraints on hydrogen generation during serpentinization of ultramafic rocks. Geochim. Cosmochim. Ac. 73, 856–875. https://doi.org/10.1016/j.gca.2008.10.032

Miller, H.M., Mayhew, L.E., Ellison, E.T., Kelemen, P., Kubo, M., Templeton, A.S., 2017. Low temperature hydrogen production during experimental hydration of partially-serpentinized dunite. Geochim. Cosmochim. Ac. 209, 161–183. https://doi.org/10.1016/j.gca.2017.04.022

Moll, M., Paulick, H., Suhr, G., Bach, W., 2007. Data report: microprobe analyses of primary phases (olivine, pyroxene, and spinel) and alteration products (serpentine, iowaite, talc, magnetite, and sulfides) in Holes 1268A, 1272A, and 1274A. In Kelemen, P.B., Kikawa, E., and Miller,

D.J. (Eds.), Proc. ODP, Sci. Results 209: College Station, TX (Ocean Drilling Program), 1–13. https://doi:10.2973/ odp.proc.sr.209.003.2007.

Myagkiy, A., Brunet, F., Popov, C., Krüger, R., Guimarães, H., Sousa, R. S., Charlet, L., Moretti, I., 2020. H_2 dynamics in the soil of a H_2-emitting zone (São Francisco Basin, Brazil): Microbial uptake quantification and reactive transport modelling. Applied Geochemistry 112, 104474. https://doi.org/10.1016/j.apgeochem.2019.104474.

Neal, C., Stanger, G., 1983. Hydrogen generation from mantle source rocks in Oman. Earth Planet. Sc. Lett. 66, 315–320. https://doi.org/10.1016/0012-821X(83)90144-9

Olowe, A.A., Génin, J.M.R., 1991. The mechanism of oxidation of ferrous hydroxide in sulphated aqueous media: Importance of the initial ratio of the reactants. Corros. Sci. 32, 965–984. https://doi.org/10.1016/0010-938X(91)90016-I

Pan, Z., Bártová, B., LaGrange, T., Butorin, S.M., Hyatt, N.C., Stennett, M.C., Kvashnina, K.O., Bernier-Latmani, R., 2020. Nanoscale mechanism of UO_2 formation through uranium reduction by magnetite. Nat. Commun. 11, 4001. https://doi.org/10.1038/s41467-020-17795-0

Petersen, J.M., Zielinski, F.U., Pape, T., Seifert, R., Moraru, C., Amann, R., Hourdez, S., Girguis, P.R., Wankel, S.D., Barbe, V., Pelletier, E., Fink, D., Borowski, C., Bach, W., Dubilier, N., 2011. Hydrogen is an energy source for hydrothermal vent symbioses. Nature 476, 176–180. https://doi.org/10.1038/nature10325

Putnis, A., 2002. Mineral replacement reactions: from macroscopic observations to microscopic mechanisms. Mineral. Mag. 66, 689–708. https://doi.org/10.1180/0026461026650056

Ruby, C., Abdelmoula, M., Naille, S., Renard, A., Khare, V., Ona-Nguema, G., Morin, G., Génin, J.-M.R., 2010. Oxidation modes and thermodynamics of FeII–III oxyhydroxycarbonate green rust: Dissolution–precipitation versus in situ deprotonation. Geochim. Cosmochim. Ac. 74, 953–966. https://doi.org/10.1016/j.gca.2009.10.030

Schwarzenbach, E.M., Caddick, M.J., Beard, J.S., Bodnar, R.J., 2016. Serpentinization, element transfer, and the progressive development of zoning in veins: evidence from a partially serpentinized harzburgite. Contrib. Mineral. Petrol. 171, 5. https://doi.org/10.1007/s00410-015-1219-3

Sharp, Z.D., Barnes, J.D., 2004. Water-soluble chlorides in massive seafloor serpentinites: a source of chloride in subduction zones. Earth Planet. Sc. Lett. 226, 243–254. https://doi.org/10.1016/j.epsl.2004.06.016

Takai, K., Gamo, T., Tsunogai, U., Nakayama, N., Hirayama, H., Nealson, K.H., Horikoshi, K., 2004. Geochemical and microbiological evidence for a hydrogen-based, hyperthermophilic subsurface lithoautotrophic microbial ecosystem (HyperSLiME) beneath an active deep-sea hydrothermal field. Extremophiles 8, 269–282. https://doi.org/10.1007/s00792-004-0386-3

Templeton, A.S., Ellison, E.T., 2020. Formation and loss of metastable brucite: does Fe(II)-bearing brucite support microbial activity in serpentinizing ecosystems? Phil. Trans. R. Soc. A 378, 20180423. https://doi.org/10.1098/rsta.2018.0423

745 Tosca, N.J., Ahmed, I.A.M., Tutolo, B.M., Ashpitel, A., Hurowitz, J.A., 2018. Magnetite authigenesis
746 and the warming of early Mars. Nature Geosci. 11, 635–639. https://doi.org/10.1038/s41561-
747 018-0203-8

748 Trolard, F., Bourrié, G., Abdelmoula, M., Refait, P., Feder, F., 2007. Fougerite, a new mineral of the
749 pyroaurite-iowaite group: description and crystal structure. Clay Clay Miner. 55, 323–334.
750 https://doi.org/10.1346/CCMN.2007.0550308

751 Turner, R.C., Hoffman, I., Chen, D., 1963. Thermogravimetry of the dehydration of $Mg(OH)_2$. Can.
752 J. Chem. 41, 243–251. https://doi.org/10.1139/v63-039

753 Turvey, C.C., Wilson, S.A., Hamilton, J.L., Tait, A.W., McCutcheon, J., Beinlich, A., Fallon, S.J.,
754 Dipple, G.M., Southam, G., 2018. Hydrotalcites and hydrated Mg-carbonates as carbon sinks
755 in serpentinite mineral wastes from the Woodsreef chrysotile mine, New South Wales,
756 Australia: Controls on carbonate mineralogy and efficiency of CO_2 air capture in mine
757 tailings. Int. J. Greenh. Gas Con. 79, 38–60. https://doi.org/10.1016/j.ijggc.2018.09.015

758 Vacher, L.G., Truche, L., Faure, F., Tissandier, L., Mosser-Ruck, R., Marrocchi, Y., 2019.
759 Deciphering the conditions of tochilinite and cronstedtite formation in CM chondrites from
760 low temperature hydrothermal experiments. Meteorit. Planet. Sci. 54, 1870–1889.
761 https://doi.org/10.1111/maps.13317

762 Yoo, M., Han, S.-J., Wee, J.-H., 2013. Carbon dioxide capture capacity of sodium hydroxide aqueous
763 solution. J. Environ. Manage. 114. https://doi.org/10.1016/j.jenvman.2012.10.061

764

Figure captions

Fig. 1. X-ray diffraction patterns of ferroan brucite (Cu*K*α radiation). (A) Synthetic product obtained by precipitation of chloride salts. (B) Natural sample from the Oman ophiolite (B). The main Bragg's reflexions of ferroan brucite are marked with vertical dashed lines. S: serpentine minerals.

Fig. 2. Back-scattered electron micrographs of the starting material and reaction products. A and B: Starting material where ferroan brucite occurs as ~ 50 to 100 nm wide platelets. C: Reaction product from PTFE reactor (Run # 15) showing ~ 400 nm wide platelets composed of the aggregation of smaller crystallites. (D) Nanometric euhedral magnetite precipitating at the surface of platelets (Run #15). mag: magnetite.

Fig. 3. X-ray diffraction patterns (Cu*Kα*) of ferroan brucite reaction products (PTFE reactors) displayed from bottom to top with increasing run duration. A: Full XRD patterns with labeled phases; B: Enlargement of [36 – 40°] 2-theta region to emphasize the shift of the (101) reflexion of ferroan brucite as the result of iron oxidation. Bragg's reflexions of ferroan and ferrian brucites are marked with vertical dashed lines and vertical long-dashed lines, respectively. Phase names as in Table 1. From bottom to top, XRD patterns correspond to ferroan brucite starting material followed by the powder XRD of Runs #06 to #10 (Table 1).

Fig. 4. Thermogravimetric analysis of the ferroan brucite starting material and of two ferrian brucite rich samples. (A) Synthetic ferroan brucite weight loss during thermogravimetric analysis (solid line). From ambient to 461 K, physisorbed water is mainly released. (B) Ferrian brucite rich sample (Run #15) weight loss during thermogravimetric analysis (dotted-dashed line). Weight loss between 461 and 505 K could be attributed to pyroaurite structural (interlayer) water loss. (C) Comparison of TGA data for starting material (solid line) and reaction products from Runs #09 (dashed line) and #15 (dotted-dashed line). (D) Weight loss first derivative (smoothed with sliding mean method) for

starting material (solid line) and reaction products from Runs #09 (dashed line) and #15 (dotted-dashed line). Heating rate: 10 K/min. For C and D, light grey zones indicate the temperature ranges where evolved CO_2 has been detected. TGA data up to 1273 K have been collected on Run #15 and no significant mass loss was observed above 873 K.

Fig. 5. Time evolution of phase proportions at 378 K as determined using quantitative phase analysis on the reaction products. Black lines: Runs #06 to #10 (ferroan brucite synthesized from Cl-solutions and reacted with ultrapure degassed water); Grey lines: Runs #01 to #03 (ferroan brucite synthesized with SO_4-solution and reacted in the synthesis solution). Abbreviations: Fe^{II}-brc: ferroan brucite; pyr: pyroaurite; mag: magnetite; Fe^{III}-brc: ferrian brucite.

Fig. 6. Eh-pH Pourbaix diagram of iron phases in a Mg-bearing aqueous system ($a_{Mg^{2+}}$ = 10^{-3} mol/L) at 378 K. The stability fields of ferroan and ferrian brucite are displayed for x = 0.2 by considering ideal solid solutions. Computations were performed with the slop16.dat database (https://gitlab.com/ENKI-portal/geopig/-/blob/master/slop/slop16.dat) and the properties for $Fe(OH)_2$ given in Klein et al. (2013). Diagrams were computed by excluding ferrian brucite (solid line), using a solid solution computed from goethite and brucite thermodynamic properties (dotted line), and for Gibbs energy of formation 10 kJ/mol below (dashed line) and above (dashed-dotted line) this latter solid solution.

Highlights

- Reaction of synthetic ferroan brucite, a serpentinization product, at temperatures below 403 K
- Ferrian brucite is formed from ferroan brucite oxidation under intermediate oxygen fugacity
- Ferrian brucite is isostructural to ferroan brucite and has the same Fe/Mg ratio
- Deprotonation of ferrian brucite layer is responsible for charge compensating Fe^{II} oxidation
- In the presence of common anions (Cl^-, CO_3^{2-}), LDHs are formed from ferroan brucite oxidation

Table 1 (Editable version)

Click here to access/download;Table (Editable version);table_1_correction4_ACS.xlsx

Run number / name	Temperature	Pressure	Duration	W/R	Ferroan brc	Pyr	Mag	Ferrian brc	Ferroan brc		Ferrian brc	
	(K)	(MPa)	(days)		(wt.%)	(wt.%)	(wt.%)	(wt.%)	xFe (mol.%)	CSD (110) (nm)	xFe (mol.%)	CSD (110) (nm)
starting material "FeBR_R0.4_S_2": salt type = SO4, ferroan brc with xFe = 21.6(3) and CSD (110) = 33(2) nm ; reactor: PTFE ; fluid: synthesis solution												
#01 / FeBR_R0.4_S_M105_8d	378	L/V	8	N.D.	89.9(8)	10.2(8)			21.7(2)	56(5)		
#02 / FeBR_R0.4_S_M105_15d	378	L/V	15	N.D.	63.8(13)	7.5(11)	0.9(2)	27.8(15)	23.5(4)	54(9)	27.8(15)	44(10)
#03 / FeBR_R0.4_S_M105_31d	378	L/V	31	N.D.	16.7(11)	8.0(15)	1.5(2)	73.8(17)	19.1(10)	57(24)	15.2(20)	51(5)
starting material "FeBR_R0.05_S": salt type = SO4, ferroan brc with xFe = 22.8(4) and CSD (110) = 33(5) nm ; reactor: PTFE ; fluid: synthesis solution												
#04 / FeBR_R0.05_S_M105_7d	378	L/V	7	N.D.	86.1(19)	0.4(1)	0.3(1)	13.3(19)	20.8(2)	62(7)	17	14(2)
#05 / FeBR_R0.05_S_M105_31d	378	L/V	31	N.D.	70.5(15)	0.3(3)	2.6(4)	26.7(15)	23.6(4)	41(5)	17	48(12)
starting material "FeBR_R0.4_Cl_2": salt type = Cl, ferroan brc with xFe = 17.4(4) and CSD (110) = 22(1) nm ; reactor: PTFE ; fluid: ultrapure degassed water												
#06 / FeBR_R0.4_Cl_1d	378	L/V	1	100	91.9(13)	6.0(13)	2.1(2)		16.6(4)	19(1)		
#07 / FeBR_R0.4_Cl_3d	378	L/V	3	100	80.4(14)	17.0(14)	2.6(2)		19.3(3)	61(10)		
#08 / FeBR_R0.4_Cl_7d	378	L/V	7	100	67.8(14)	17.3(14)	3.6(2)	11.3(10)	19.0(3)	95(22)	17	16(2)
#09 / FeBR_R0.4_Cl_15d	378	L/V	15	100	52.9(12)	13.5(16)	3.7(2)	29.9(11)	20.2(4)	71(17)	16.1(30)	40(5)
#10 / FeBR_R0.4_Cl_36d*	378	L/V	36	100	5.8(11)	30.6(14)	2.9(3)	60.7(17)	20	14(5)	19.3(36)	58(11)
starting material "FeBR_R0.05_Cl": salt type = Cl, ferroan brc with xFe = 19.4(3) and CSD (110) = 30(2) nm ; reactor: PTFE ; fluid: ultrapure degassed water												
#11 / FeBR_R0.05_Cl_1d	403	L/V	1	100	77.6(8)	19.8(8)	2.6(2)		20.1(3)	68(10)		
#12 / FeBR_R0.05_Cl_3d	403	L/V	3	100	72.8(8)	24.0(8)	3.2(3)		18.9(3)	60(8)		
#13 / FeBR_R0.05_Cl_7d	403	L/V	7	100	75.4(7)	19.6(7)	4.0(2)	1.0(3)	18.1(2)	76(12)	17	
#14 / FeBR_R0.05_Cl_15d	403	L/V	15	100	59.4(8)	22.9(6)	3.8(2)	13.9(9)	17.5(2)	104(23)	17	23(3)
#15 / FeBR_R0.05_Cl_31d	403	L/V	31	100	22.8(9)	24.3(7)	3.8(2)	49.4(10)	19.3(6)	31(4)	17.1(25)	105(24)
#16 / FeBR_R0.05_Cl_w-r25_3d	403	L/V	3	25	90.0(6)	7.0(5)	3.0(2)		18.8(3)	41(5)		
starting material "FeBR_R0.4_Cl_7_centrifugation": salt type = Cl, ferroan brc with xFe = 16.2(4) and CSD (110) = 24(2) nm ; reactor: gold capsule ; fluid: ultrapure degassed water												
#17 / FeBR_R0.4_Cl_caps1_105deg_15d	378	20	15	3.13	91.5(19)	5.4(19)	3.2(2)		11.0(4)	44(3)		
#18 / FeBR_R0.4_Cl_caps2_105deg_26d	378	20	26	3.23	95.7(4)	0.4(3)	3.9(3)		13.3(6)	16(1)		
starting material "FeBR_R0.4_Cl_10": salt type = Cl, ferroan brc with xFe = 19.1(5) and CSD (110) = 17.1(8) nm ; reactor: PTFE ; fluid: ultrapure degassed water												
#19 / FeBR_R0.4_Cl_10_32d	378	L/V	32	100	9.5(15)	16.6(9)	5.9(4)	68.0(18)	20		13.9(32)	53(10)
starting material "FeBR_R0.4_Cl_11": salt type = Cl, ferroan brc with xFe = 20.5(4) and CSD (110) = 17.9(8) nm ; reactor: PTFE ; fluid: ultrapure degassed water												
#20 / FeBR_R0.4_Cl_11_32d	378	L/V	32	100	17.8(4)	10.3(7)	4.2(3)	67.7(16)	19.3(12)	46(17)	18.0(28)	38(4)

Table 1. List of all experiments sorted by starting material and experimental setup. Mass proportions, xFe and grain sizes are inferred from Rietveld refinement. Numbers in parentheses are standard deviations associated with the refinement. W/R: water to rock ratio ; Ferroan brc: brucite containing Fe(II) ; Pyr: pyroaurite ; Mag: magnetite ; Ferrian brc: brucite containing Fe(III) ; xFe = Fetot/Fetot+Mg ; SO_4 : sulfate salts used for ferroan brucite synthesis ; Cl : chloride salts used for ferroan brucite synthesis ; R : see text ; * : starting material "FeBR_R0.4_Cl_5": salt type = Cl, ferroan brc with x = 23.1(6) and CSD (110) = 14(1) nm

Figure 1

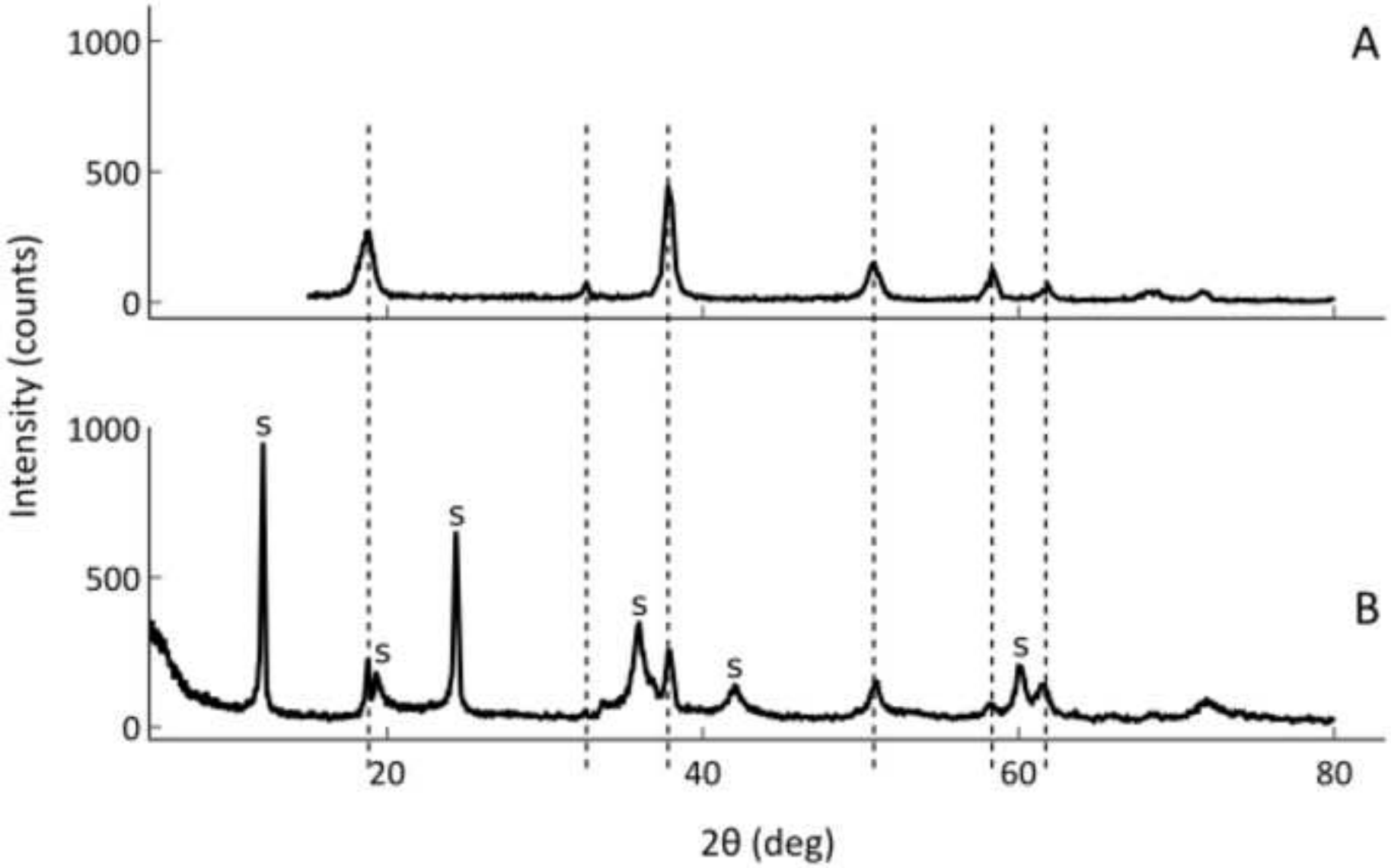

Figure 2

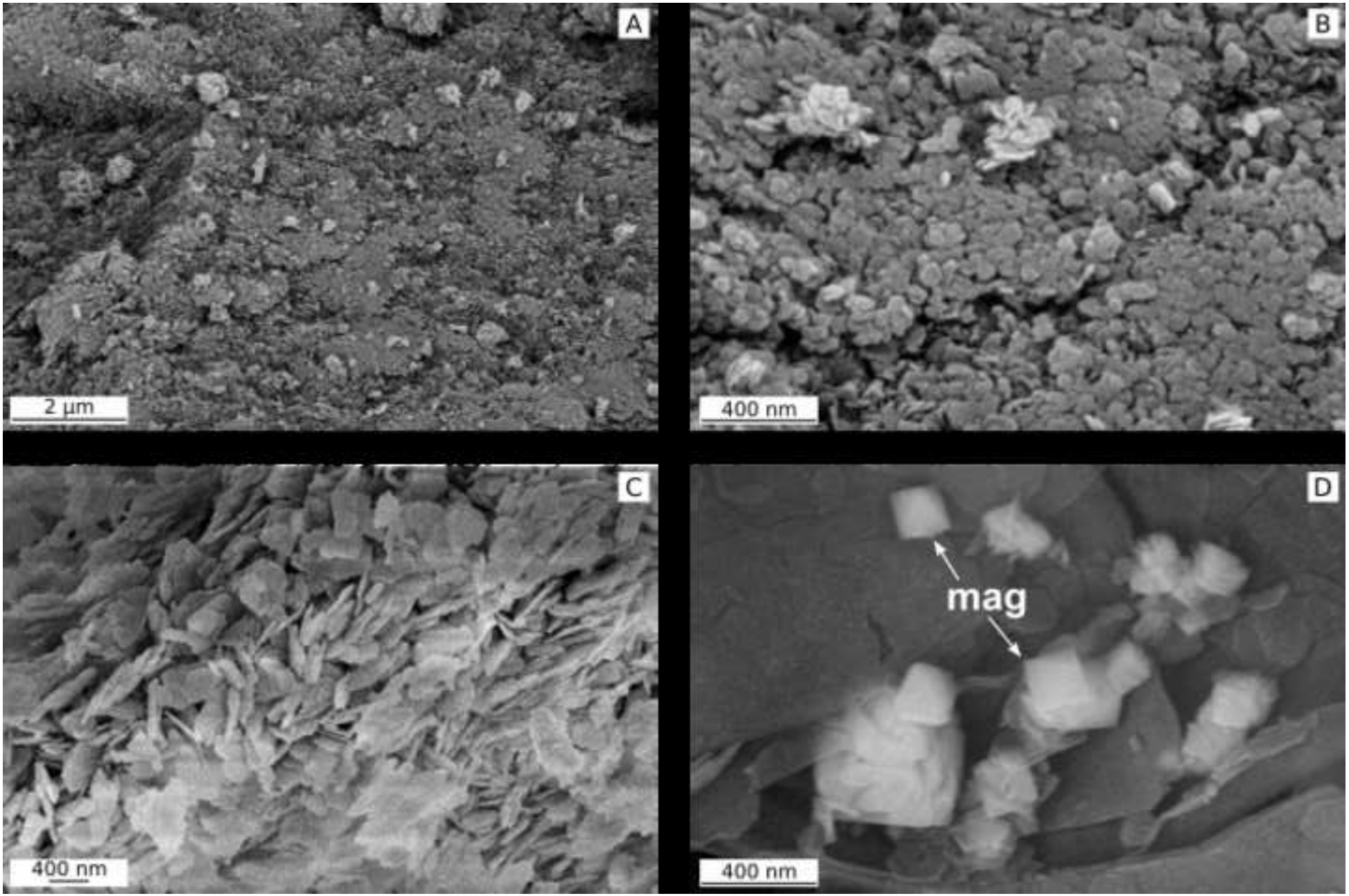

Figure 3

Click here to access/download;Figure;XRD_105_teflon_oneplot_small+zoom_38deg_v2.png

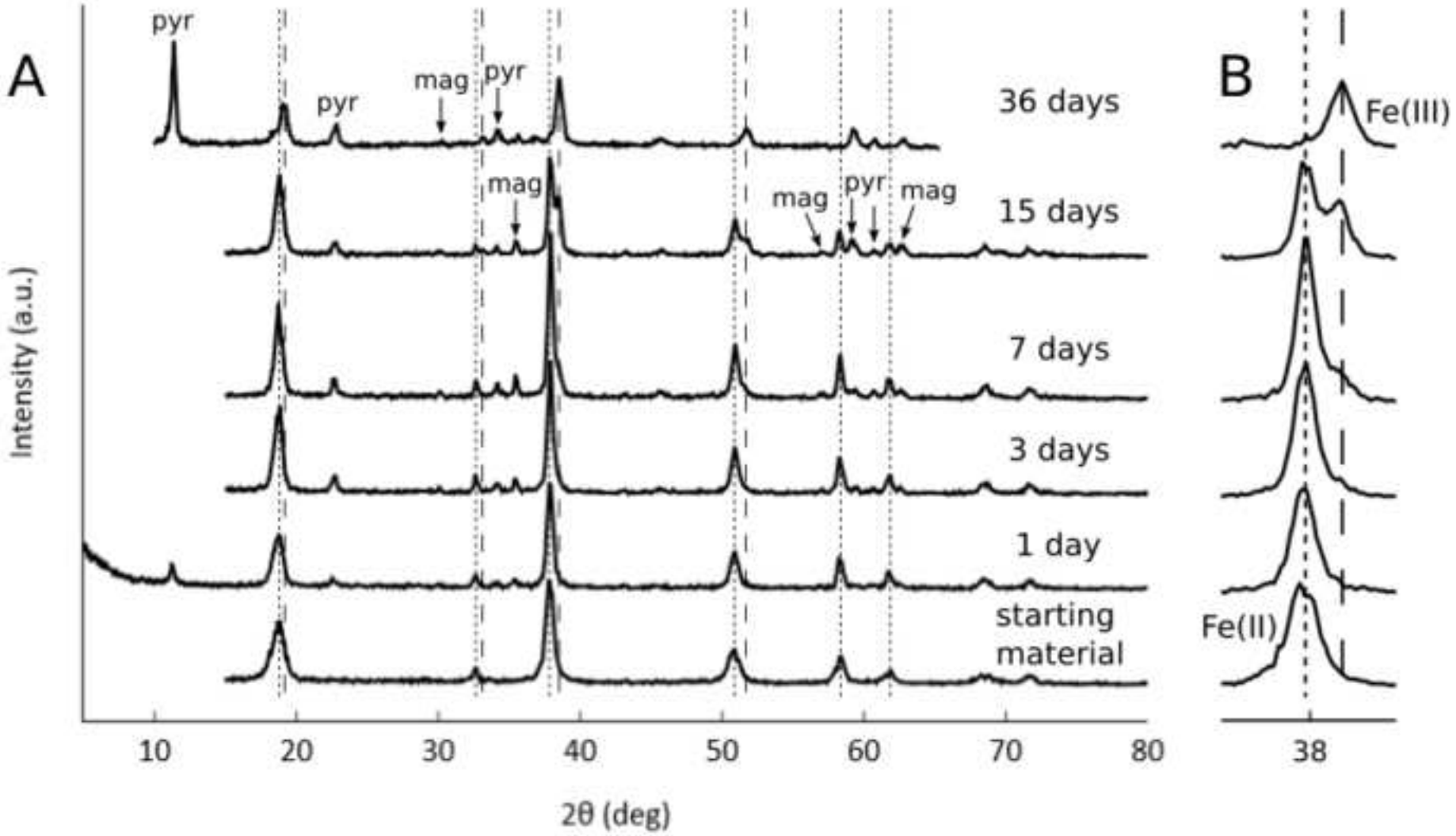

Figure 4

Click here to access/download;Figure;TG_and_DTG_and_anoted_weightloss_

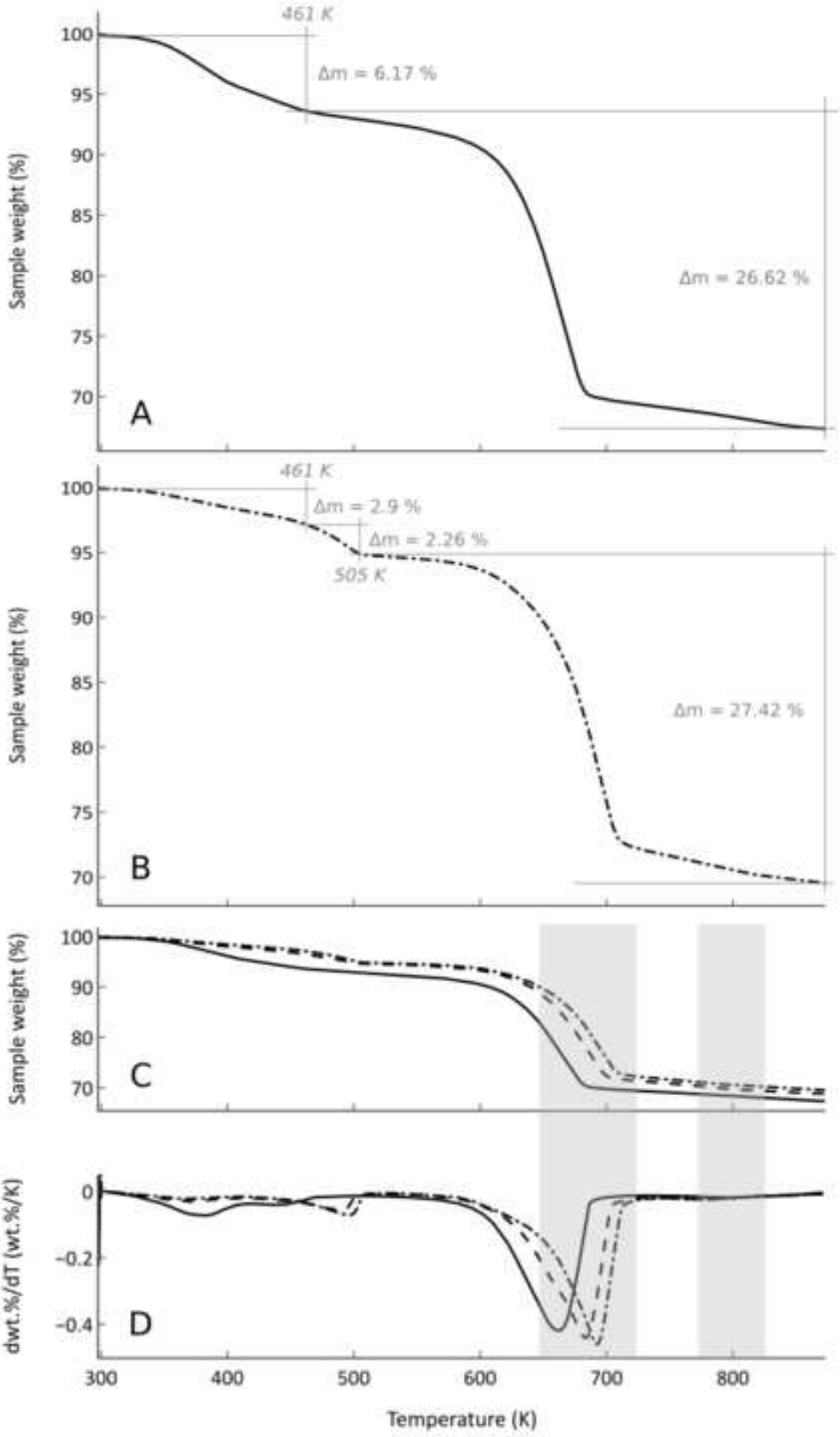

Figure 5

Click here to access/download;Figure;phase_proportions_PTFE_378K_article_legend_correction3.

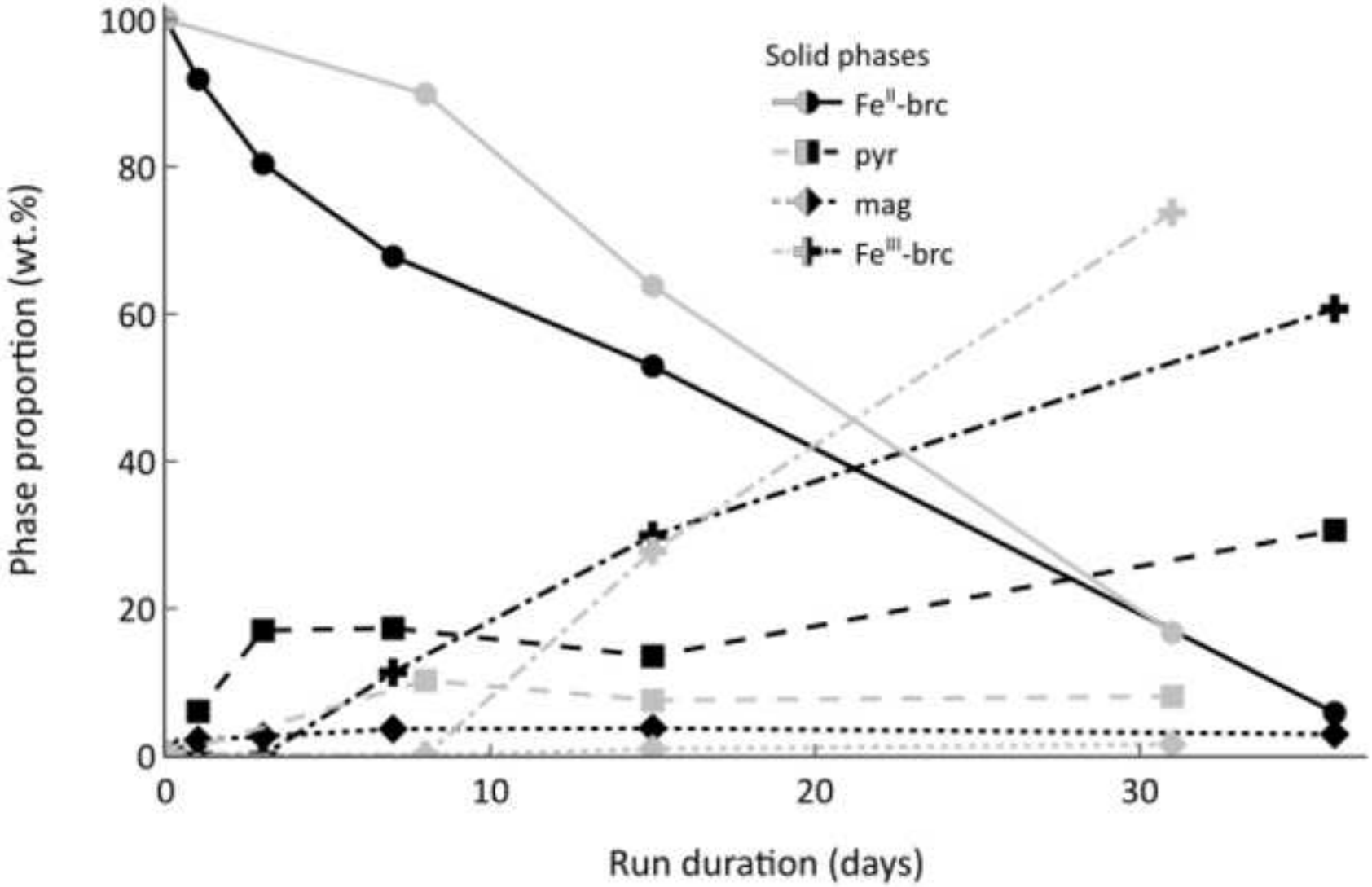

Figure 6

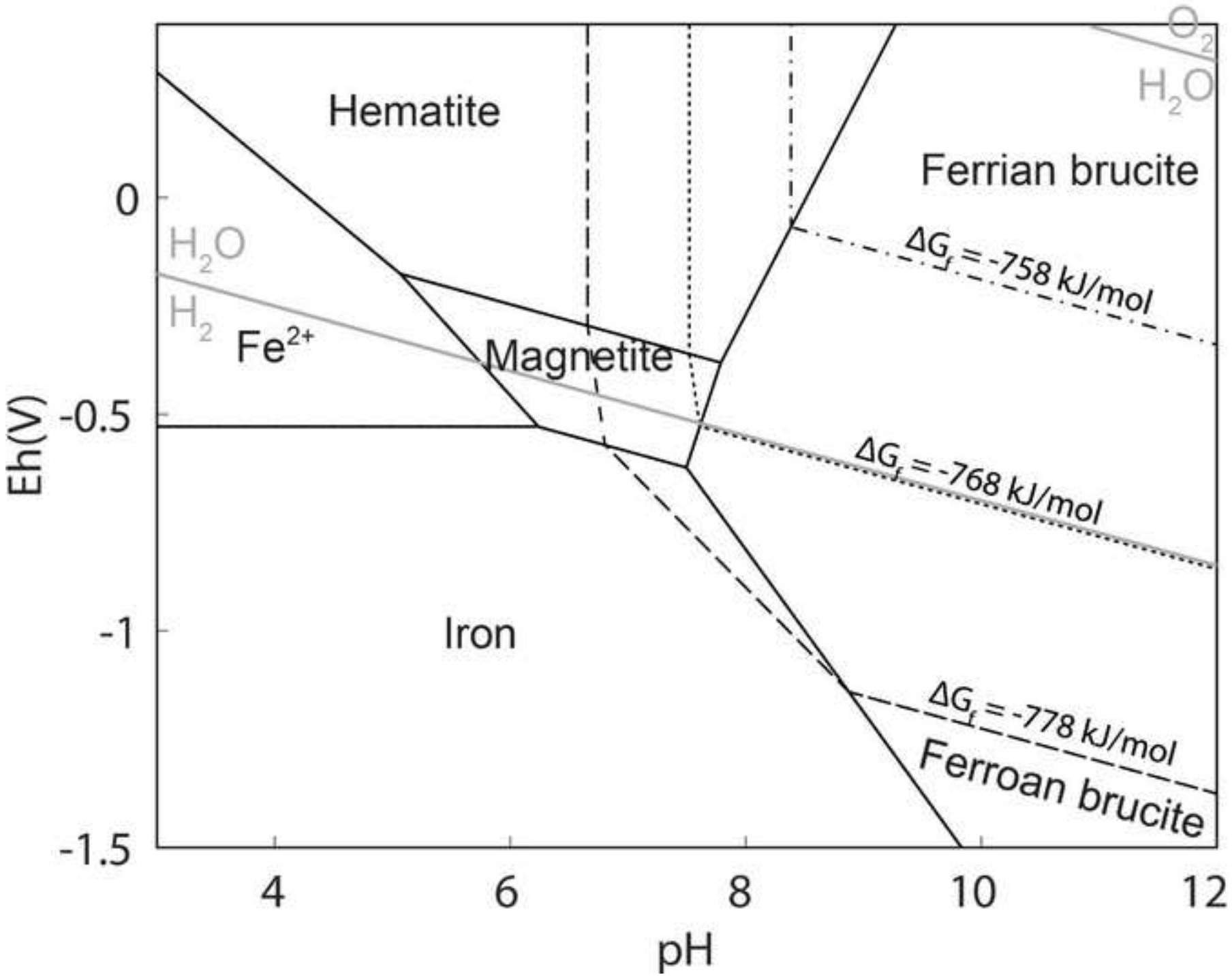

Fe^{III}-substituted brucite: hydrothermal synthesis from $(Mg_{0.8},Fe^{II}_{0.2})$-brucite, crystal chemistry and relevance to the alteration of ultramafic rocks

William Carlin[1,2], Benjamin Malvoisin[1], Bruno Lanson[1], Fabrice Brunet[1], Nathaniel Findling[1], Martine Lanson[1], Valérie Magnin[1], Tiphaine Fargetton[2], Laurent Jeannin[2], Olivier Lhote[3]

[1] Univ. Grenoble Alpes, USMB, CNRS, IRD, UGE, ISTerre, France

[2] Storengy (ENGIE), France

[3] Engie Research, ENGIE, France

Supplementary information

Details for Rietveld refinements on ferroan and ferrian brucite

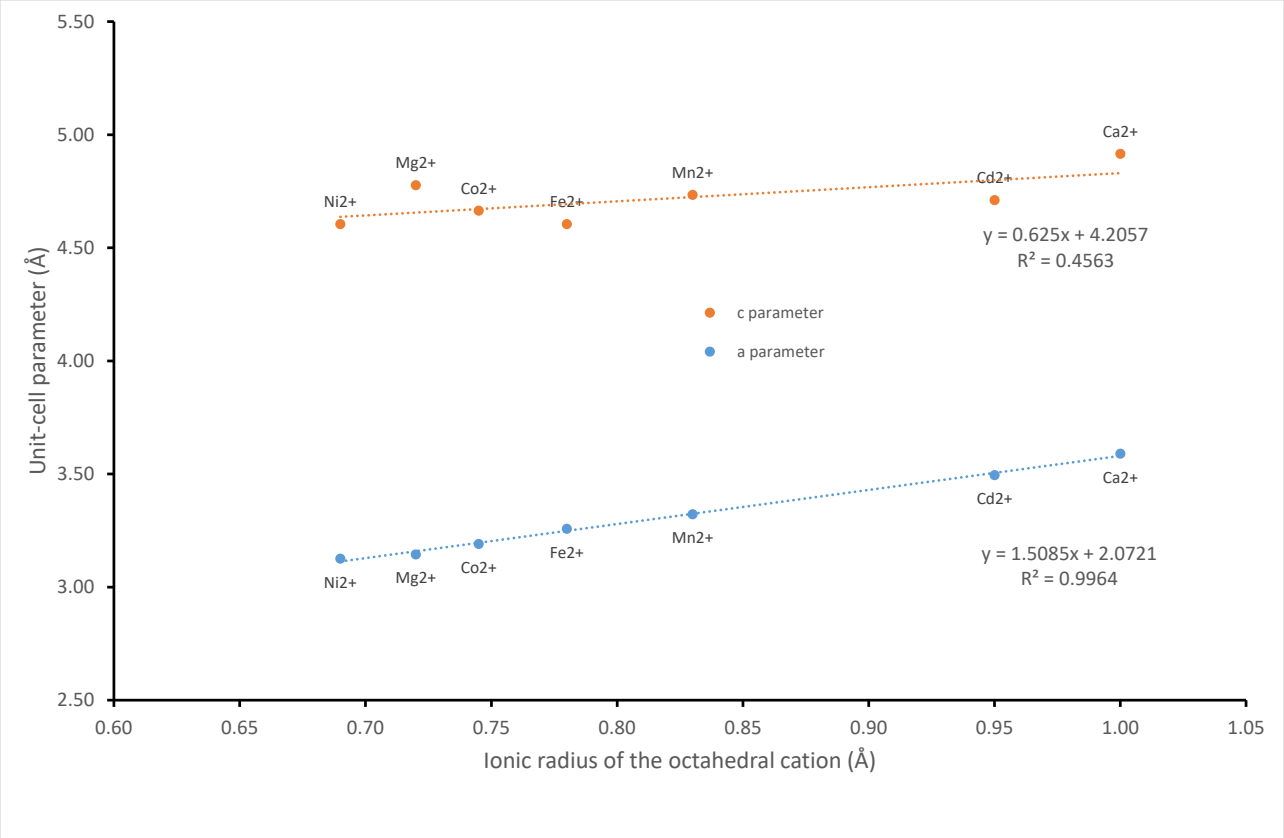

Fig. S1. Evolution of in-plane *a* and out-of-plane *c* unit-cell parameters in brucite-like structures as a function of the ionic radius of octahedral cation. Ionic radii from Shannon (1976). Unit-cell parameters from ICDD database: portlandite-$Ca(OH)_2$ #44-1481; $Cd(OH)_2$ #31-228; pyrochroite-$Mn(OH)_2$ #1-73-1133; β-$Co(OH)_2$ #30-443; brucite-$Mg(OH)_2$ #44-1482; theophrastite-$Ni(OH)_2$ #14-117; amakinite-$Fe(OH)_2$ from Wyckoff (1963).

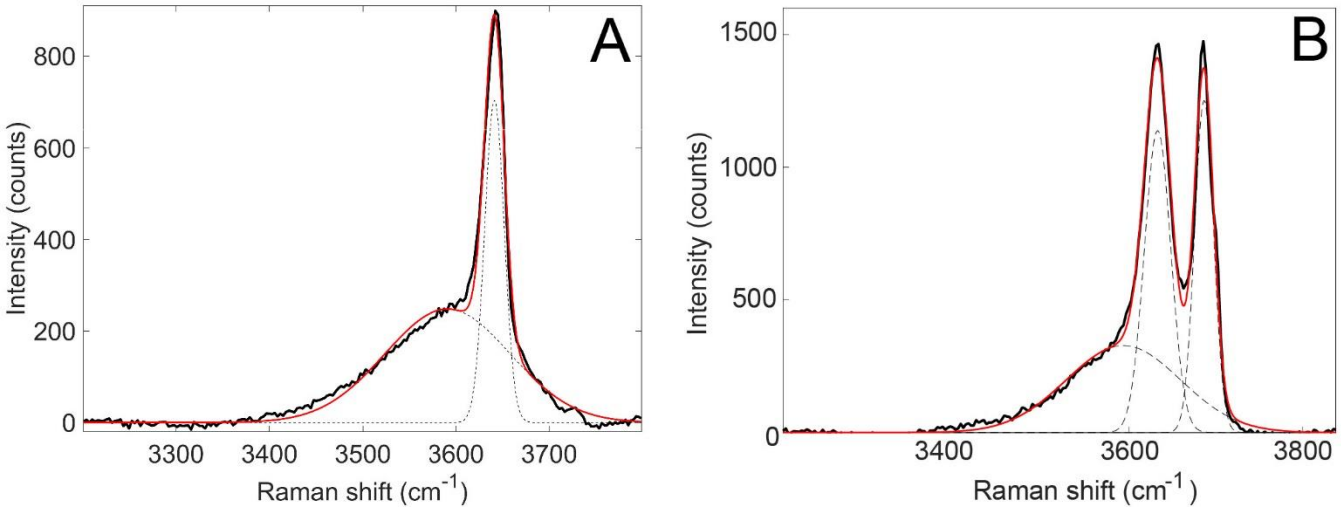

Fig. S2. Raman spectra of (A) synthetic and (B) natural ferroan brucites. The spectra were fitted with Lorentzian functions (dashed lines), and their sum is displayed with the solid red curve. The peak at 3641 cm^{-1} in A and at 3632 cm^{-1} in B was attributed to the ν_1 OH-stretching band of ferroan brucite. Its position is used to determine the Fe content of ferroan brucite (*x***)** using the calibration of Templeton and Ellison (2020). The broad peak at ~ 3590 cm^{-1} was attributed to ferroan brucite oxidation in air during measurement. **A**. Synthetic ferroan brucite (sample FeBR_R0.4_Cl_11) for which $x = 0.17 \pm 0.05$ (from Raman spectroscopy). **B**. Oman sample BA4A-81-1-1-17 for which $x = 0.287 \pm 0.03$. The peak at 3686 cm^{-1} with a shoulder at 3700 cm^{-1} (Auzende et al., 2004) corresponds to lizardite that is intermixed with ferroan brucite at the submicrometer scale.

Implications of the Fe^{III} and Fe^{II} determination performed on Runs #19 and #20

Both starting material and reaction products of Runs #19 and #20 have been analyzed for their Fe^{III} and Fe^{II} contents (Fig. S3). The starting material of Run #19 has been aged in the glove box until a thin reddish film was visible. The Fe^{III} content of this starting material can thus be considered as an upper bound. For comparison, the starting material of Run #20 has been prepared with the same care with respect to O_2 contamination as all the other starting materials used in this study. Despite this care, ~ 8 wt. % of Fe^{III} is present in the starting material.

Assuming that all Fe^{III} present in the starting material would readily produce magnetite, an expected wt.% of magnetite for Runs #19 and #20, of 6.4 and 2.9 is calculated which compares relatively well with the magnetite content derived from Rietveld analysis of the XRPD data of 5.9 and 4.2 wt.%, respectively.

The expected Fe^{III}/Fe_{tot} ratio in Runs #19 and #20 can be calculated from the Rietveld analysis of the XRPD data (Table S4) which provides both phase compositions and proportions. Pyroaurite composition was assumed to be ideal (Mg:Fe ratio of 3:1) because the refined value of its in-plane unit-cell parameter *a* scatters very little [3.1112(13)-3.1170(70) for all samples with > 10% pyroaurite – data not shown] close to the ideal 3.109 Å value.

For the run product of Run #19, Fe^{III}/Fe_{tot} = 0.82(9) to be compared with the measured value of 0.92(6) (Fig. S3). For Run #20, Fe^{III}/Fe_{tot} = 0.79(6) to be compared with the measured value of 0.87(5) (Fig. S3). The Fe^{III} and Fe^{II} contents of Runs #19 and #20 are therefore in good agreement with the phase composition/structural model that has been used for Rietveld refinement.

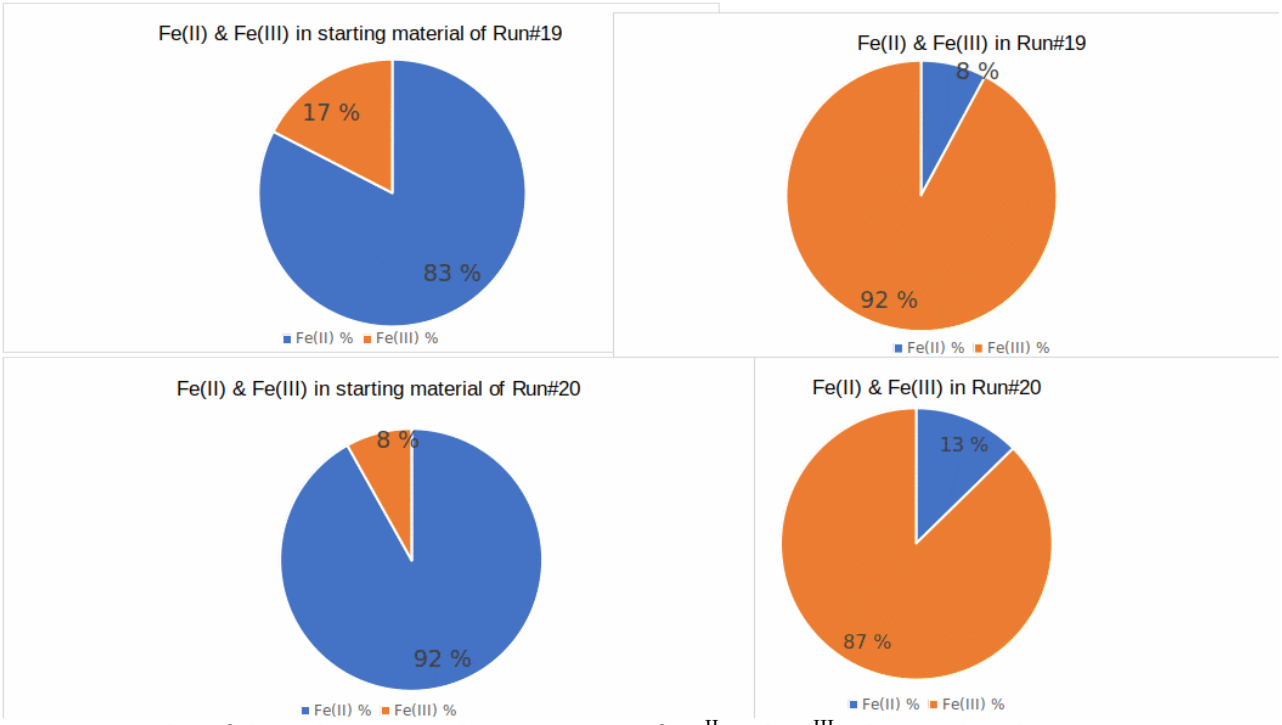

Fig. S3. Results of the colorimetric determination of Fe^{II} and Fe^{III} relative abundances in starting materials (left) and reaction products (right) for Runs #19 and #20 (top and bottom, respectively).

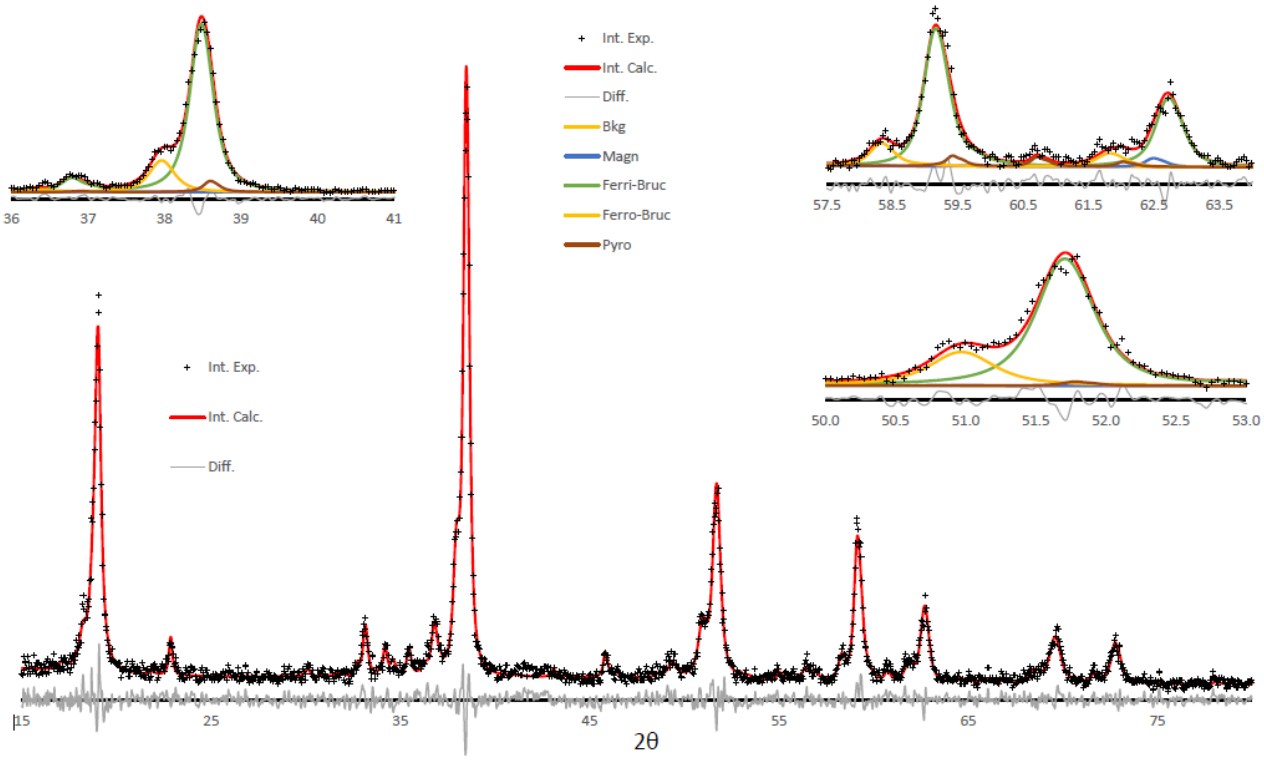

Fig. S4. Rietveld refinement of X-ray diffraction data from Run #03 reaction products. Zoomed frames show the contribution of each phase. *Int. Exp.*: Measured intensity; *Int. Calc.*: Calculated intensity; *Diff.*: Difference between measured and calculated intensities; *Bkg*: Background

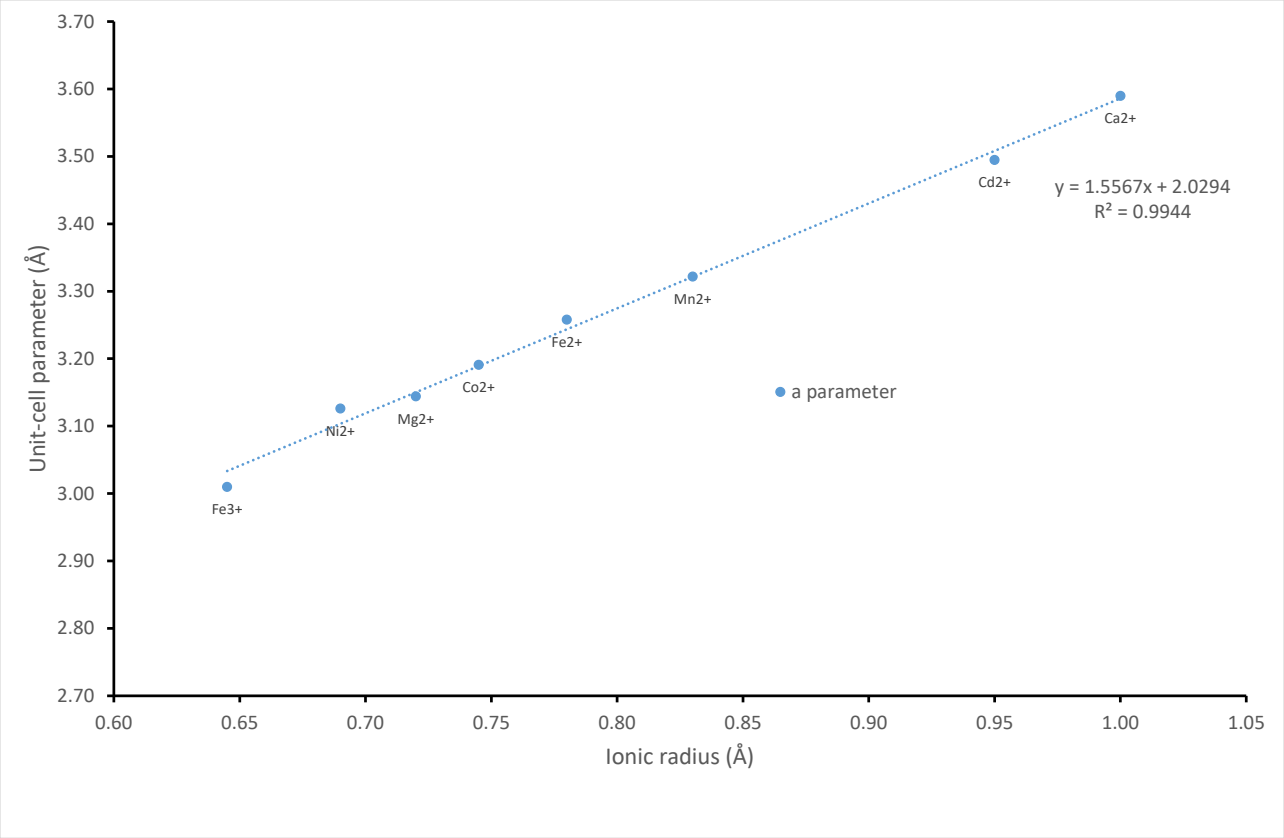

61

62 **Fig. S5.** Extension of the regression between in-plane *a* unit-cell parameters of brucite-like structures

63 and the ionic radius of divalent octahedral cation to include Fe^{III}. Values for divalent cations as in

64 Fig. S1; unit-cell parameters for fully oxidized green rust ($Fe^{III}_6O_{12}H_8CO_3$) from Génin et al. (2006).

Table S1. Crystal parameters refined for ferroan and ferrian brucite and Rietveld refinement details.

Phase / Sample	*a* (Å)	*c* (Å)	*V* (Å³)	Z	R_p (%)	R_{wp} (%)	R_{exp} (%)	*GoF*
Ferroan brucite (s.g. #164 $P\bar{3}m1$)								
FeBR_R0.4_S_2	3.1699(4)	4.744(1)	41.29	1	12.2	16.1	18.2	0.88
FeBR_R0.4_Cl_2	3.1651(6)	4.751(2)	41.22	1	15.9	21.0	17.9	1.18
Ferrian brucite (s.g. #164 $P\bar{3}m1$)								
#03 / FeBR_R0.4_S_M105-2_31d	3.1255(5)	4.6774(13)	39.57	1	10.3	13.5	16.6	0.82
#10 / FeBR_R0.4_Cl_36d	3.1259(5)	4.6759(18)	39.57	1	11.8	15.2	15.6	0.97

Notes: *a* and *c*: Unit-cell parameters; *V*: Cell volume; *Z*: Formula units per cell; *Rp*: Unweighted profile R-factor; *Rwp*: Weighted profile R-factor; *Rexp*: Expected R-factor ; *GoF*: Goodness of fit.

Table S2. Fractional atomic coordinates, isotropic displacement parameters and selected interatomic bond distances (Å) for ferroan and ferrian brucite.

Phase / Sample	Site - Position	*x*	*y*	*z*	B_{iso} (Å^2)	*Occ.*	(Mg1,Fe1)-O1 (Å)
Ferroan brucite / FeBR_R0.4_S_2	Mg1 – 1a	0	0	0	0.48	0.774(4)	
	Fe^{II}1 – 1a	0	0	0	0.48	0.226(4)	2.121(8)
	O1 – 2d	1/3	2/3	0.226(3)	0.82	1	
Ferroan brucite / FeBR_R0.4_Cl_2	Mg1 – 1a	0	0	0	0.48	0.816(5)	
	Fe^{II}1 – 1a	0	0	0	0.48	0.184(5)	2.139(8)
	O1 – 2d	1/3	2/3	0.234(3)	0.82	1	
Ferrian brucite	Mg1 – 1a	0	0	0	0.48	0.842(20)	
#03 / FeBR_R0.4_S_M105-2_31d	Fe^{III}1 – 1a	0	0	0	0.48	0.152(20)	2.087(8)
	O1 – 2d	1/3	2/3	0.224(3)	0.82	1	
Ferrian brucite	Mg1 – 1a	0	0	0	0.48	0.807(36)	
#10 / FeBR_R0.4_Cl_36d	Fe^{III}1 – 1a	0	0	0	0.48	0.193(36)	2.080(10)
	O1 – 2d	1/3	2/3	0.221(4)	0.82	1	

Table S3. Results of the Rietveld refinements performed on reaction products from all experiments.

Run number / Sample name	Ferrian brucite				Fit quality estimates		
	a param. (Å)	c param. (Å)	z (fraction of c param.)	CSD 110 (nm)	Rwp	Rexp	GoF
#01 / FeBR_R0.4_S_M105_8d					16.6	17.9	0.93
#02 / FeBR_R0.4_S_M105_15d	3.1276(8)	4.6703(24)	0.222	44(10)	19.4	19.0	1.02
#03 / FeBR_R0.4_S_M105_31d	3.1255(5)	4.6774(13)	0.224(3)	51(5)	13.5	16.6	0.82
#04 / FeBR_R0.05_S_M105_7d	3.1383(39)	4.7157(31)	0.222	14(2)	14.7	18.4	0.8
#05 / FeBR_R0.05_S_M105_31d	3.1354(9)	4.6891(32)	0.222	48(12)	21.3	20.2	1.06
#06 / FeBR_R0.4_Cl_1d					18.3	17.6	1.03
#07 / FeBR_R0.4_Cl_3d					16.3	18.0	0.91
#08 / FeBR_R0.4_Cl_7d	3.1298(19)	4.6674(41)	0.222	16(2)	15.6	17.0	0.92
#09 / FeBR_R0.4_Cl_15d	3.1244(56)	4.6723(20)	0.222	40(5)	15.1	18.2	0.83
#10 / FeBR_R0.4_Cl_36d	3.1259(5)	4.6759(18)	0.221(4)	58(11)	15.2	15.6	0.97
#11 / FeBR_R0.05_Cl_1d					17.8	19.9	0.89
#12 / FeBR_R0.05_Cl_3d					18.2	19.7	0.92
#13 / FeBR_R0.05_Cl_7d	3.1167(24)	4.6712(41)	0.222		16.1	18.9	0.85
#14 / FeBR_R0.05_Cl_15d	3.1282(12)	4.6789(37)	0.222	23(3)	15.5	17.8	0.87
#15 / FeBR_R0.05_Cl_31d	3.1294(5)	4.6817(12)	0.220(3)	105(24)	17.0	18.9	0.90
#16 / FeBR_R0.05_Cl_w-r25_3d					15.4	18.1	0.85
#17 / FeBR_R0.4_Cl_caps1_105deg_15d					18.2	18.5	0.98
#18 / FeBR_R0.4_Cl_caps2_105deg_26d					15.3	17.4	0.88
#19 / FeBR_R0.4_Cl_10_32d	3.1273(6)	4.6859(21)	0.218(4)	53(10)	29.6	28.7	1.03
#20 / FeBR_R0.4_Cl_11_32d	3.1246(7)	4.6733(21)	0.226(4)	38(4)	29.8	28.2	1.05

Note: a and *c*: ferrian brucite unit-cell parameters (space group $P\bar{3}m1$); *z*: z-coordinate of the O atom 2d position (space group $P\bar{3}m1$); CSD: size of the coherent scattering domains along 110; *Rwp*: Weighted profile R-factor; *Rexp*: Expected R-factor ; *GoF*: Goodness of fit.

Table S4. Fe^{III}/Fe_{tot} ratio calculated from phase composition and relative proportions derived from the quantitative phase analysis of reaction products from Runs #19 & #20.

Mineral	Structural formula	Rel. Prop. wt.%	nFe^{2+}	nFe^{3+}
Ferroan Brucite	$Mg_{0.8}Fe_{0.2}(OH)_2$	9.5(15)	0.029	
Pyroaurite	$Mg_6Fe^{3+}_2(OH)_{16}[CO_3]\ 4.5H_2O$	16.6(9)		0.049
Ferrian Brucite	$Mg_{0.86}Fe_{0.14}O_{0.14}(OH)_{1.86}$	68.0(18)		0.151
Magnetite	$Fe^{2+}O{\cdot}Fe^{3+}_2O_3$	5.9(4)	0.025	0.051
		Sum	0.055(6)	0.252(10)
Run #19			Fe^{3+}/Fe_{tot}	**0.82(9)**

Mineral	Formula	Rel. Prop. wt.%	nFe^{2+}	nFe^{3+}
Ferroan Brucite	$Mg_{0.81}Fe_{0.19}(OH)_2$	17.8(4)	0.052	
Pyroaurite	$Mg_6Fe^{3+}_2(OH)_{16}[CO_3] \cdot 4.5H_2O$	10.3(7)	0	0.031
Ferrian Brucite	$Mg_{0.82}Fe_{0.18}O_{0.18}(OH)_{1.82}$	67.7(16)	0	0.191
Magnetite	$Fe^{2+}O{\cdot}Fe^{3+}_2O_3$	4.2(3)	0.018	0.036
		Sum	0.070(3)	0.258(9)
Run #20			Fe^{3+}/Fe_{tot}	**0.79(6)**

References

Auzende, A. L., Daniel, I., Reynard, B., Lemaire, C., Guyot, F. (2004). High-pressure behaviour of serpentine minerals: a Raman spectroscopic study. Phys. Chem. Miner., 31, 269-277. https://doi.org/10.1007/s00269-004-0384-0

Génin, J.-M.R., Ruby, C., Upadhyay, C., 2006. Structure and thermodynamics of ferrous, stoichiometric and ferric oxyhydroxycarbonate green rusts; redox flexibility and fougerite mineral. Solid State Sci 8, 1330–1343. https://doi.org/10.1016/j.solidstatesciences.2006.05.010

Shannon, R.D., 1976. Revised effective ionic radii and systematic studies of interatomic distances in halides and chalcogenides. Acta Cryst A 32, 751–767. https://doi.org/10.1107/S0567739476001551

Templeton, A.S., Ellison, E.T., 2020. Formation and loss of metastable brucite: does Fe(II)-bearing brucite support microbial activity in serpentinizing ecosystems? Phil. Trans. R. Soc. A. 378, 20180423. https://doi.org/10.1098/rsta.2018.0423

Wyckoff, R.W.G., 1963. Crystal structures. Interscience publishers New York.